

Online supplement to 'On the analytic approximation of bulk collision rates of non-spherical hydrometeors'

Axel Seifert¹, Ulrich Blahak², and Renko Buhr³

¹Hans-Ertel Centre for Weather Research, Deutscher Wetterdienst, Hamburg, Germany

²Deutscher Wetterdienst, Offenbach, Germany

³Universität Hamburg, Hamburg, Germany

⁴Max Planck Institute for Meteorology, Hamburg, Germany

Abstract. The supplement provides further details and auxiliary figures on the analytic approximation of bulk collision rates of non-spherical hydrometeors.

KC05 result is shown here only for comparison. The numerical reference solutions used in this study does also apply the power law approximation of the fall speed for those species. Figure 3 gives an overview of the terminal fall velocities of all species used in this study. Note that not all species are physically reasonable over the whole size range shown in this plot. Nevertheless, as all the bulk integrals are for simplicity integrated from zero to infinity we have not restricted the individual graphs to the physically meaningful size range of the particles.

Note that, following the aerodynamic theory of KC05, the terminal fall velocity of arbitrary non-spherical hydrometeors will always show a functional relationship which is better fitted by an Atlas-type relation than by the simpler power law. Whether the power law is sufficient, like in our case for the cloud ice in form of hexagonal plates, depends, among other things, on the size range which is considered as physically reasonable. If we would want to include very large plates of several centimeters in diameter, the Atlas-type relation would become necessary for this particle type as well.

3 Particle size distributions

For the particle size distributions (PSDs) we assume the generalized gamma distribution w.r.t. particle mass

$$f(x) = Ax^\nu \exp(-Bx^\xi) \quad (3)$$

and the shape parameters ν and ξ are given in Table 1 of the main text. As discussed in the main text, we use the Atlas-type fall velocity ansatz

$$v_j(D_{eq}) = \alpha_j - \beta_j \exp(-\gamma_j D_{eq}) \quad (4)$$

for raindrops and snowflakes. This makes it necessary that the PSD has a similar dependency on D_{eq} , i.e., the PSD has to be a gamma distribution in equivalent diameter

$$f(D_{eq}) = N_0 D_{eq}^\mu \exp(-\lambda D_{eq}). \quad (5)$$

1 Introduction

Here we provide some further, mostly technical details, more results and auxiliary figures which are not shown in the main text, but may nevertheless be interesting for some readers.

2 Geometries and terminal fall velocities

The (fractal) geometry is given by a mass-size relation

$$x_j = a_j D_j^{b_j} \quad (1)$$

where x_j is the particle mass and D_j the maximum dimension, i.e., in SI units a_j has units of kg m^{-b_j} . Sometimes it is more convenient to use the particle mass as internal coordinate instead of the diameter, then we need the inverse relation

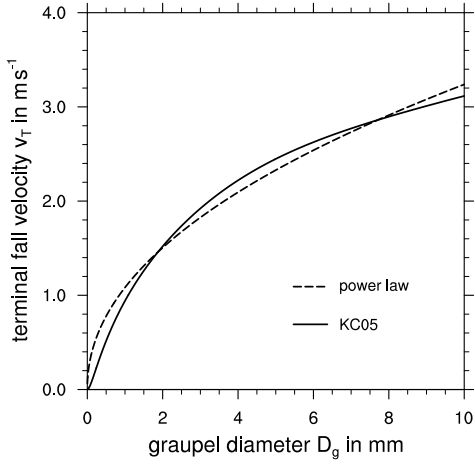
$$D_j = \hat{a}_j x_j^{\hat{b}_j} \quad (2)$$

with $\hat{b}_j = 1/b_j$ and $\hat{a}_j = (1/a_j)^{\hat{b}_j}$.

Figures 1 and 2 show the terminal fall velocity of graupel, hail and cloud ice using the Khvorostyanov and Curry (2002, 2005) theory, which acts here as a reference, and the approximation with a simple power law ansatz. The parameters of the power laws are given in Table 1 of the main text. For graupel, hail and cloud ice the power law provides a good approximation and there would be no clear advantage in using an Atlas-type relation. For these three particle species the

Correspondence to: Dr. Axel Seifert, Max-Planck-Institut für Meteorologie, Bundesstr. 53, 20146 Hamburg, Germany. E-mail: axel.seifert@dwd.de

a) terminal fall velocity of graupel



b) terminal fall velocity of hail

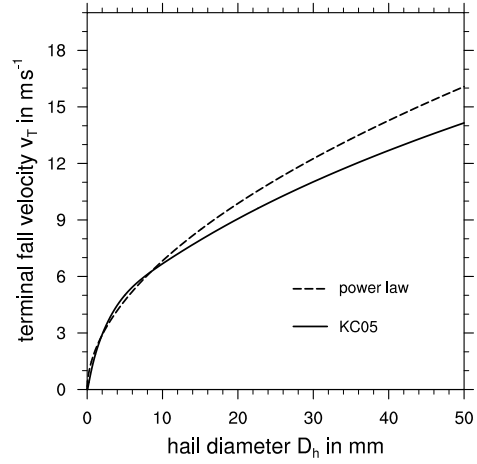


Fig. 1. Terminal fall velocity of graupel and hail. Shown are the results of the aerodynamics theory of Khvorostyanov and Curry (2002, 2005) and the power law approximation which is used for the parameterization of the bulk collision rates.

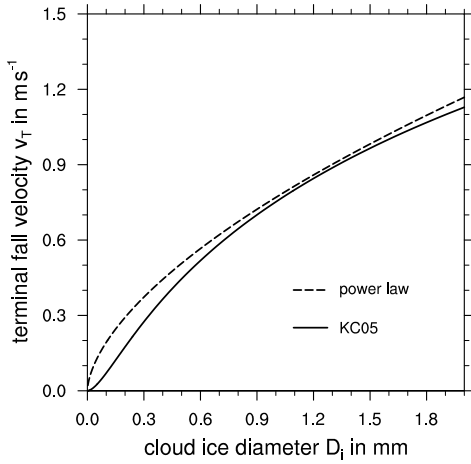


Fig. 2. As Fig. 1, but for cloud ice assuming hexagonal plates.

This can be achieved by choosing $\xi = 1/3$ and with $x = (\pi/6)\rho_w D_{eq}^3$ and

$$f(x)dx = f(D_{eq})dD_{eq} \quad (6)$$

this leads to

$$\nu = \frac{\mu - 2}{3} \quad (\text{for } \xi = 1/3) \quad (7)$$

for the shape parameter ν of the generalized gamma distribution. For particles like graupel which can be approximated with power law fall speeds, we are free to choose other values for ξ than $1/3$ and, e.g., for $\xi = 1$ a corresponding gamma distribution in D_{eq} does not exist.

4 Collision rates of different binary interactions

The Figs. 4-33 show the results for the bulk collision rates of various interactions. The Figs. 4-7 of the paper are repeated here again (as Figs. 4-7 of this supplement), but here the Wisner approximation using the Atlas-type fall velocities is explicitly included in the comparison. In Figs. 20-33 we show the symmetric percentage error

$$\text{SPE}_{\phi,ij}(D_i, D_j) = \frac{\mathcal{K}_{\phi,ij,\text{para}} - \mathcal{K}_{\phi,ij,\text{num}}}{\mathcal{K}_{\phi,ij,\text{para}} + \mathcal{K}_{\phi,ij,\text{num}}}, \quad (8)$$

i.e., the average of the absolute value of the SPE is the symmetric mean absolute percentage error (SMAPE).

Especially interesting are two cases: The collision of hail and snow is an example of an interaction which has virtually no local minimum in the collision rate, i.e., for reasonably-sized hail the snow is always falling slower than the hailstones. For this case the SB2006 parameterization and the most simple Wisner approximation using the power law fall speeds give the smallest RMSE and SMAPE errors (see Fig. 9 of the main text). The reason is that those parameterization give the best asymptotic estimate of the collision rate for large hail, and, although the collision rates are normalized, the error measures are dominated by this asymptotic regime. Nevertheless, for this interaction the most simple Wisner approximation or even a continuous growth formulation might be the method of choice when it comes to computational efficiency.

The other very interesting case is the collision of cloud ice and snow, and here the simpler approaches fail miserably, even the Wisner approximation with the Atlas-type fall speed gives very large errors. Due to the fact that the fall speeds of these two species are quite similar the new variance approxi-

mation is the only parameterization approach which provides useful bulk collision rates for this interaction.

Note that the Figs. 8 and 9 for the rain-snow interaction are only a different visualization of the results shown in the main text, i.e., the plots shows the behavior as a function of the equivalent diameter of snow instead of the raindrop diameter.

Overall these additional figures support our conclusion that the revised variance approach can provide more accurate bulk collision rates than previous analytic parameterizations. The only exception is the collection of hail and snow.

5 Optimization of the calibration exponent m

As mentioned in section 4 of the main text, we can use the calibration exponent m in the ansatz for the velocity difference, Eq. (16) of the main text,

$$\overline{\Delta v_{n,ij}} = \left\{ \frac{1}{\mathcal{N}_{n,ij}} \int_0^\infty \int_0^\infty [v_i(D_i) - v_j(D_j)]^2 \times D_i^2 D_j^2 f_i^m(x_i) f_j^m(D_j) x_j^n dD_i dx_j \right\}^{\frac{1}{2}} \quad (9)$$

to optimize the results for the bulk collision rates. Figure 34 gives a visual impression of the effect of m between values of 1 and 2.5 for two examples, namely the graupel-rain and snow-rain interactions. It can be seen that increasing m leads to a shift of the minimum in the bulk collision rate to larger diameters. For the mass collection rates the best agreement is found for values of m around 1.5, while higher values, e.g. 2, give better results for the number rate. A quantitative evaluation using RMSE and SMAPE for the eight collection rates of this study is given by Figs. 35 and 36. From these plots we found the best estimates for m for each bulk collision rate as given in Table 1 of this supplement. The Figs. 7-9 of the main text and Figs. 4-15 of this supplement show this results for those values of m . Please note that these values depend on the actual choices for the particle geometries and the associated fall speeds.

Without the tuning of the exponent m for each individual collision rate the variance approximation does nevertheless give reasonable results. As recommended in the main text one may use $m = 1.5$ for mass and $m = 2$ for number rates, if a more detailed comparison against a reference solution is not available. With the exception of the hail-snow interaction, which has been discussed above, the resulting approximations are still quite satisfactory and superior to the other parameterizations (at least when using SMAPE as the primary error metric) as shown by Fig. 37.

6 Conclusions

The additional figures presented in this supplement support the conclusions of the main text.

Table 1. Optimal values for the calibration exponent m for each bulk collision rate.

	mass	number
graupel-rain	1.6	2.0
graupel-snow	1.5	1.0
hail-rain	1.0	1.5
hail-snow	1.0	1.0
ice-rain	1.5	2.0
ice-snow	2.0	1.0
snow-rain	1.5	2.0
snow selfcollection	-	1.0

Acknowledgements. This research was carried out as part of the Hans Ertel Centre for Weather Research. This research network of Universities, Research Institutes and the Deutscher Wetterdienst is funded by the BMVBS (Federal Ministry of Transport, Building and Urban Development).

References

- Khvorostyanov, V. and Curry, J.: Terminal velocities of droplets and crystals: Power laws with continuous parameters over the size spectrum, *J. Atmos. Sci.*, 59, 1872–1884, 2002.
- Khvorostyanov, V. and Curry, J.: Fall velocities of hydrometeors in the atmosphere: Refinements to a continuous analytical power law, *J. Atmos. Sci.*, 62, 4343–4357, 2005.

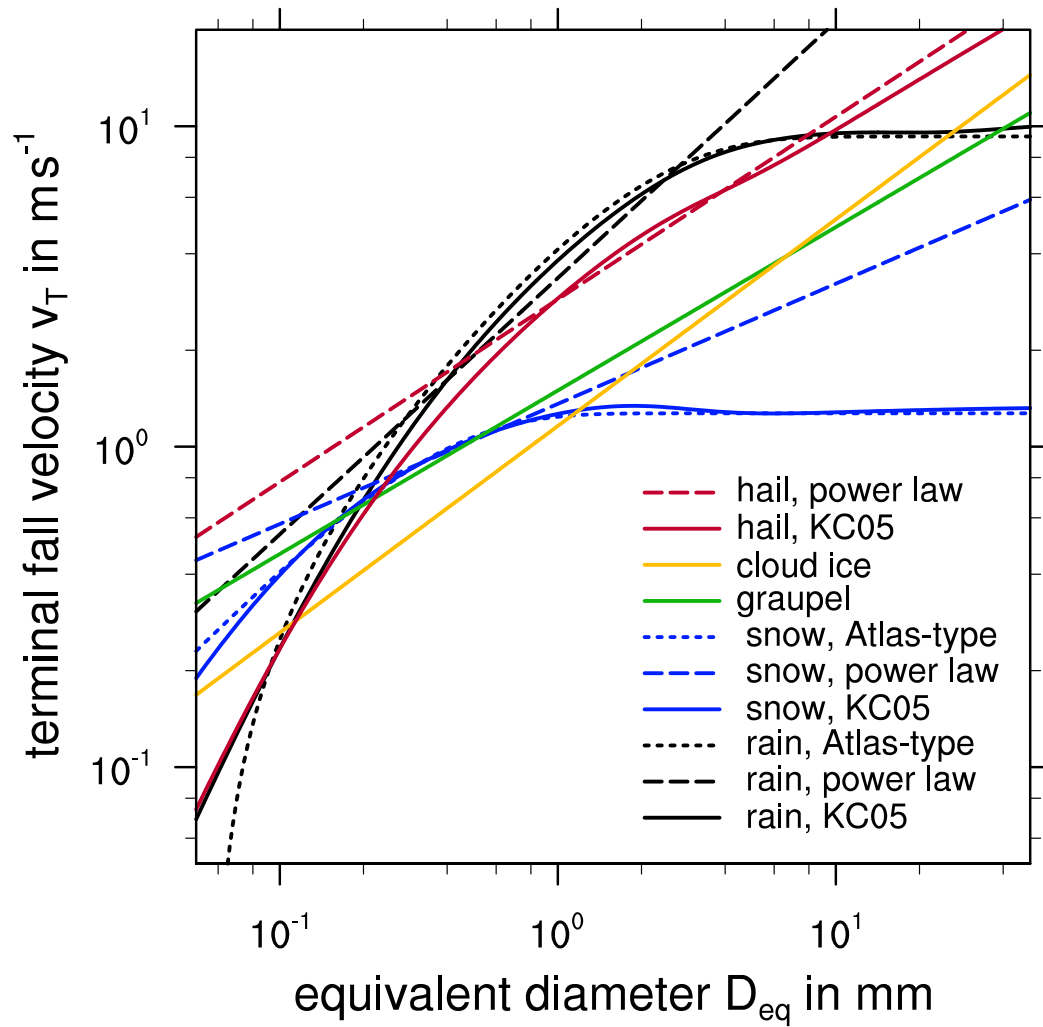
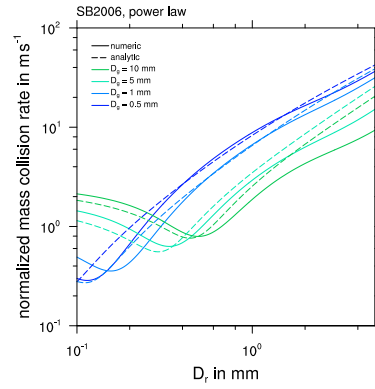
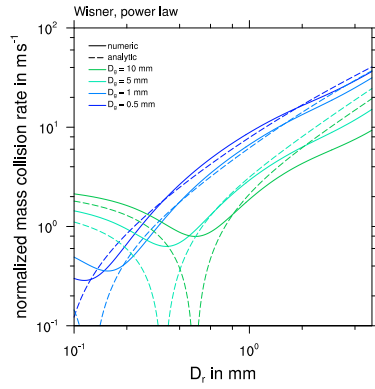


Fig. 3. Terminal fall velocities of all species as a function of equivalent diameter.

a) Wisner approx. using power-law

b) SB2006 using power-law



c) Wisner approx. using Atlas-type

d) Murakami-Mizuno using Atlas-type

e) Variance approx. using Atlas-type

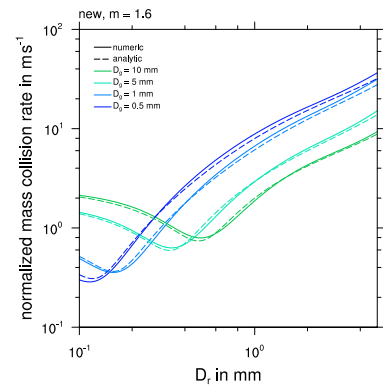
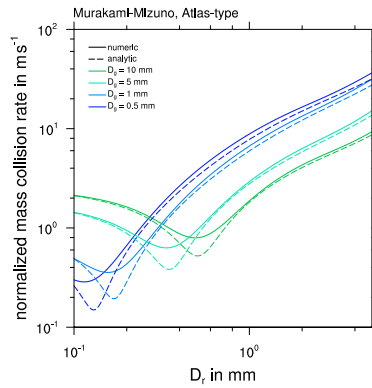
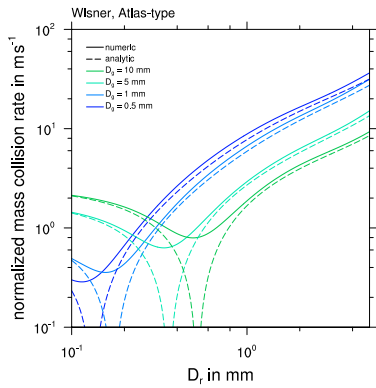
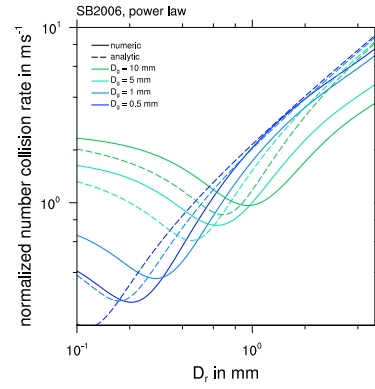
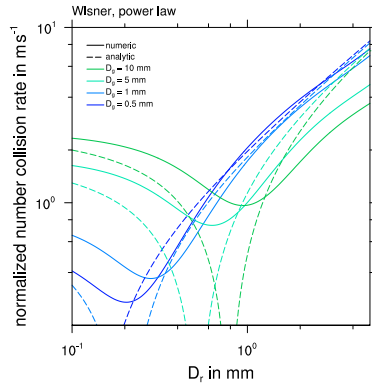


Fig. 4. Normalized mass collision rate for **graupel** and **rain** using different approximations (dashed) compared to a numerical solution of the collision integral (solid) as a function of the raindrop mean volume diameter for different mean volume diameters of the graupel size distribution.

a) Wisner approx. with power-law

b) SB2006 using power-law



c) Wisner approx. with Atlas-type

d) Murakami-Mizuno with Atlas-type

e) Variance approx. using Atlas-type

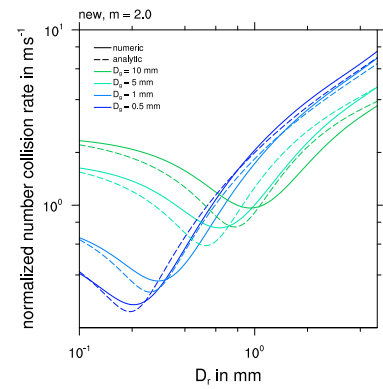
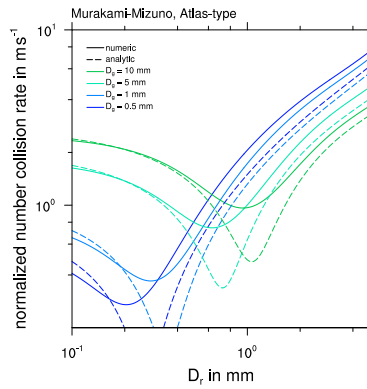
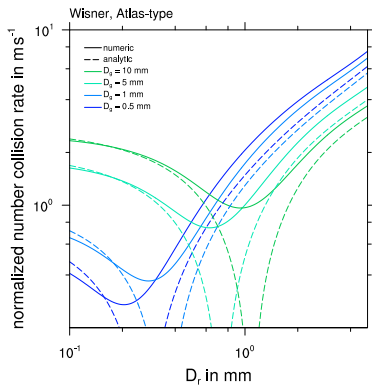
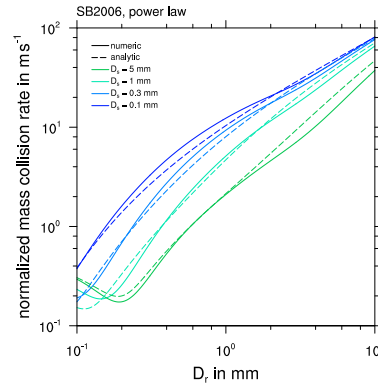
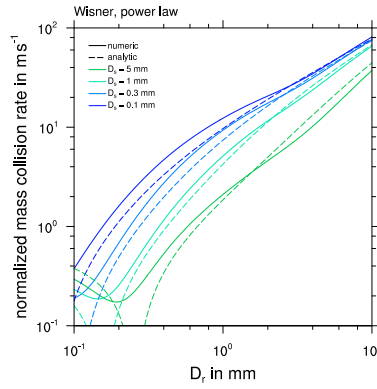


Fig. 5. As previous Figure, but showing the normalized number collision rate for **graupel** and **rain**.

a) Wisner approx. using power-law

b) SB2006 using power-law



c) Wisner approx. using Atlas-type

d) Murakami-Mizuno using Atlas-type

e) Variance approx. using Atlas-type

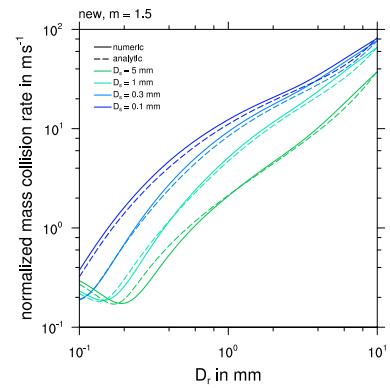
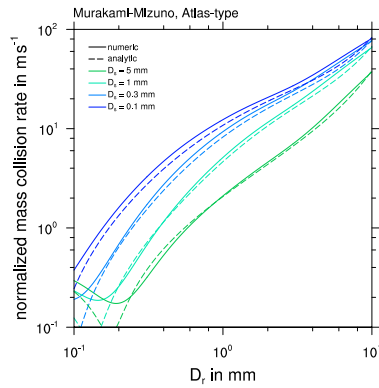
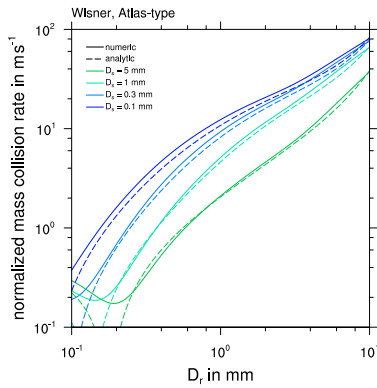
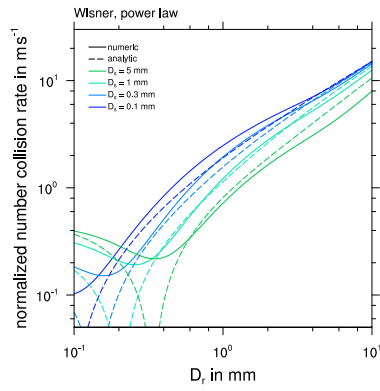
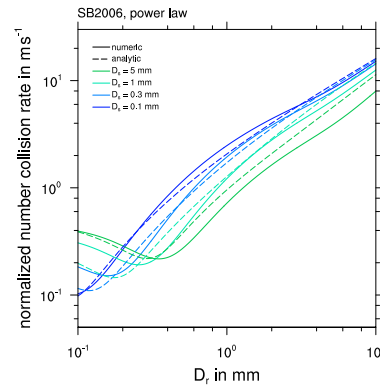


Fig. 6. Normalized mass collision rate for **snow** and **rain** using different approximations (dashed) compared to a numerical solution of the collision integral (solid) as a function of the raindrop mean volume diameter for different mean volume diameters of the snow size distribution.

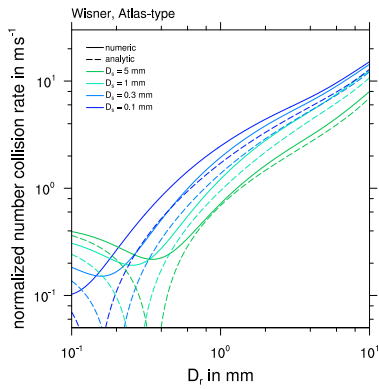
a) Wisner approx. with power-law



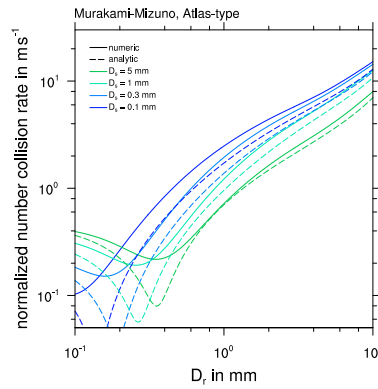
b) SB2006 using power-law



c) Wisner approx. with Atlas-type



d) Murakami-Mizuno with Atlas-type



e) Variance approx. using Atlas-type

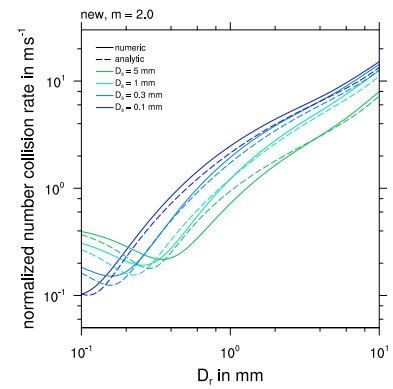
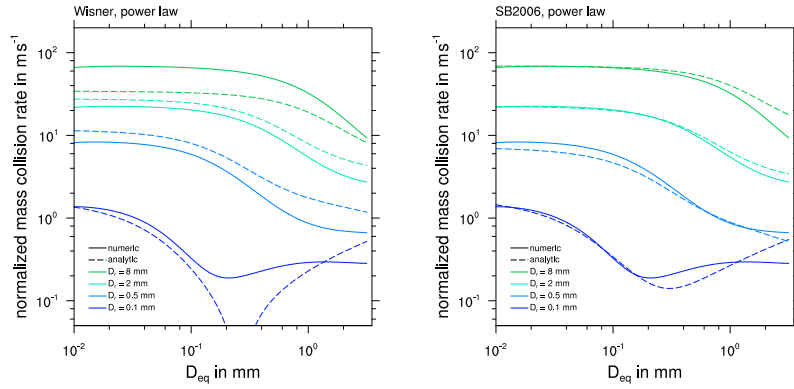


Fig. 7. As previous Figure, but showing the normalized number collision rate for **snow** and **rain**.

a) Wisner approx. using power-law

b) SB2006 using power-law



c) Wisner approx. using Atlas-type

d) Murakami-Mizuno using Atlas-type

e) Variance approx. using Atlas-type

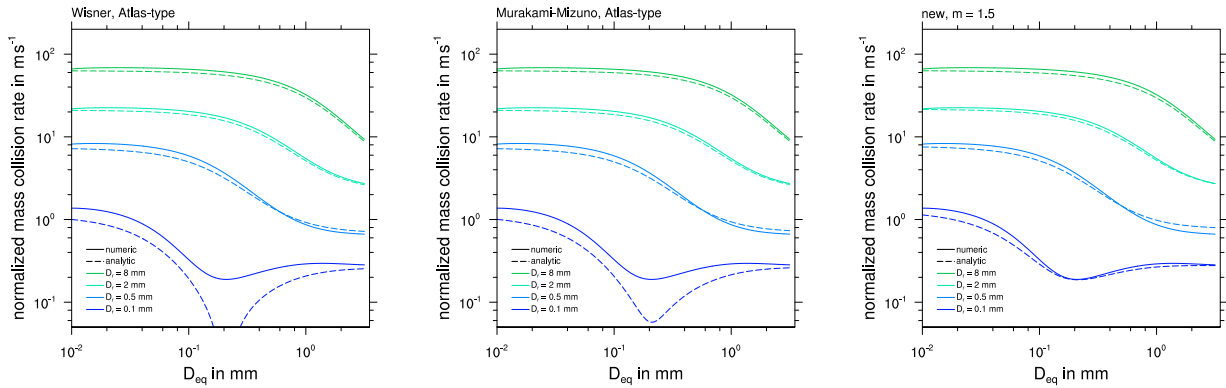
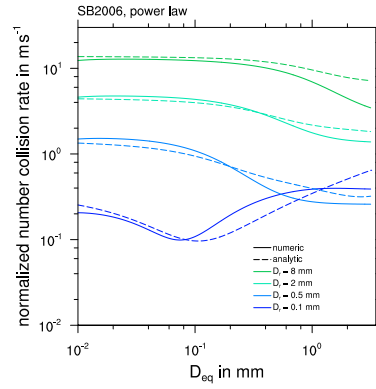
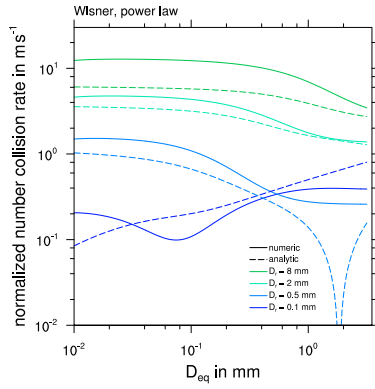


Fig. 8. Normalized mass collision rate for **rain** and **snow** using different approximations (dashed) compared to a numerical solution of the collision integral (solid) as a function of the equivalent mean volume diameter of snowflakes for different mean volume diameters of the rain size distribution. Note that this is the same data as Fig. 6 of this supplement, but here shown with the equivalent diameter of snowflakes on the abscissa.

a) Wisner approx. with power-law

b) SB2006 using power-law



c) Wisner approx. with Atlas-type

d) Murakami-Mizuno with Atlas-type

e) Variance approx. using Atlas-type

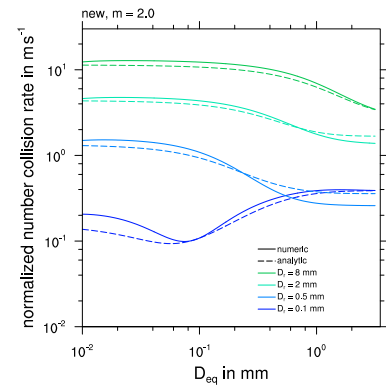
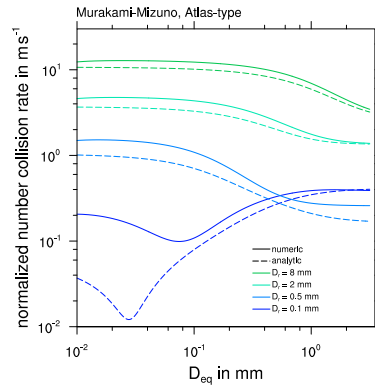
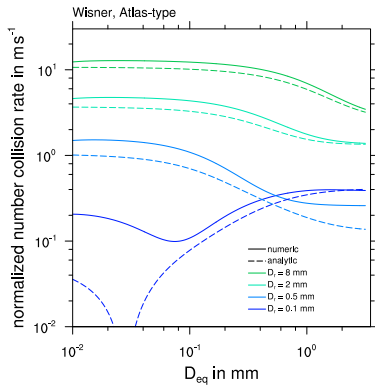
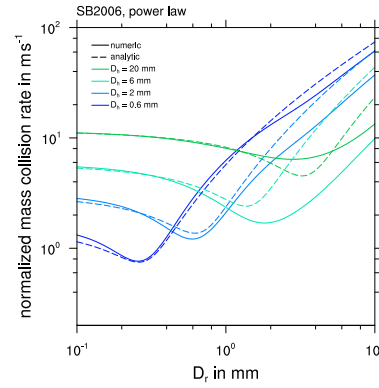
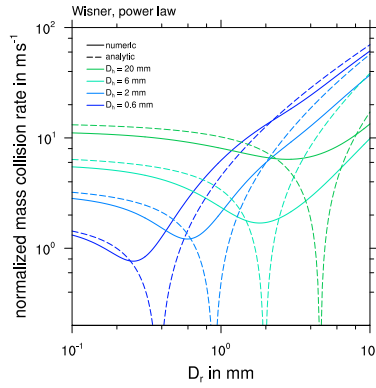


Fig. 9. As previous Figure, but showing the normalized number collision rate for **rain** and **snow**.

a) Wisner approx. using power-law

b) SB2006 using power-law



c) Wisner approx. using Atlas-type

d) Murakami-Mizuno using Atlas-type

e) Variance approx. using Atlas-type

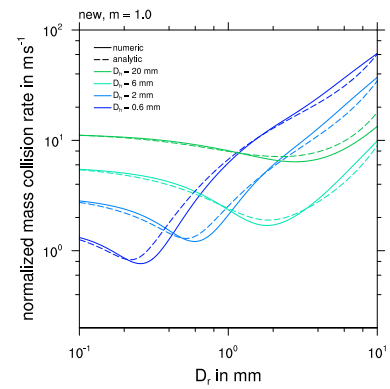
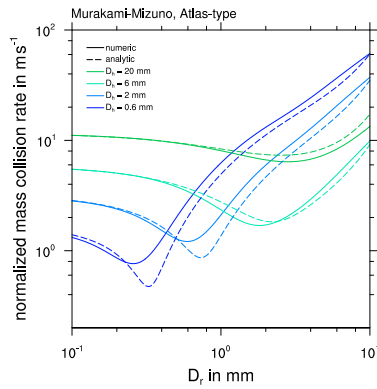
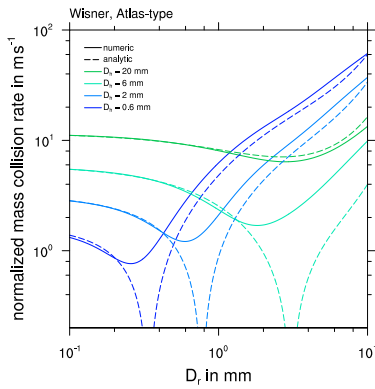
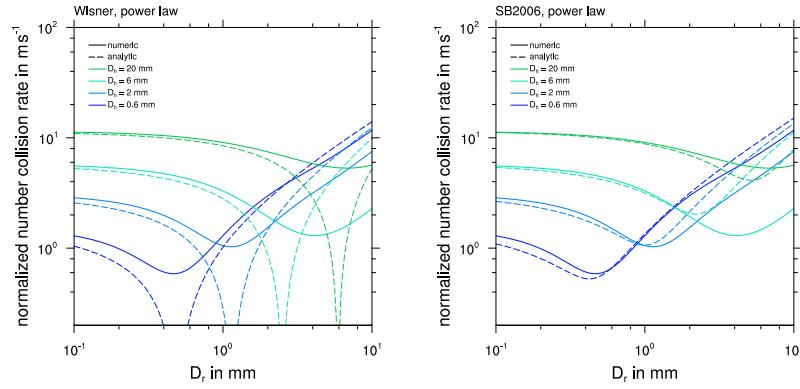


Fig. 10. Normalized mass collision rate for **hail** and **rain** using different approximations (dashed) compared to a numerical solution of the collision integral (solid) as a function of the raindrop mean volume diameter for different mean volume diameters of the hail size distribution.

a) Wisner approx. with power-law

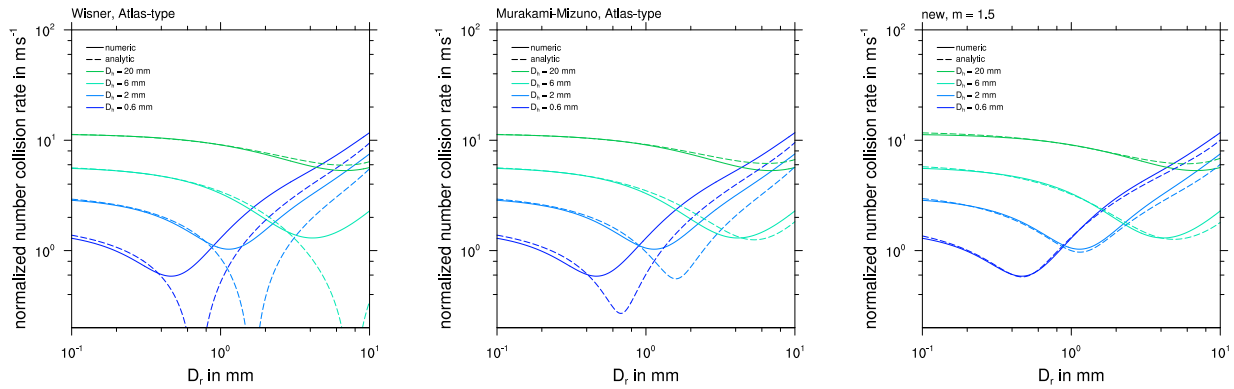
b) SB2006 using power-law



c) Wisner approx. with Atlas-type

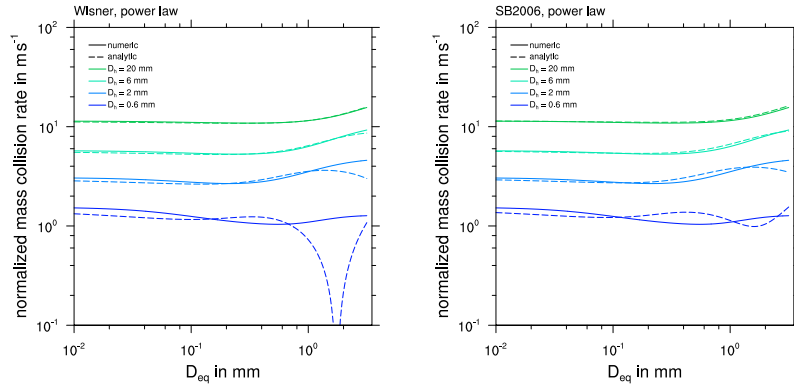
d) Murakami-Mizuno with Atlas-type

e) Variance approx. using Atlas-type

**Fig. 11.** As previous Figure, but showing the normalized number collision rate for **hail** and **rain**.

a) Wisner approx. using power-law

b) SB2006 using power-law



c) Wisner approx. using Atlas-type

d) Murakami-Mizuno using Atlas-type

e) Variance approx. using Atlas-type

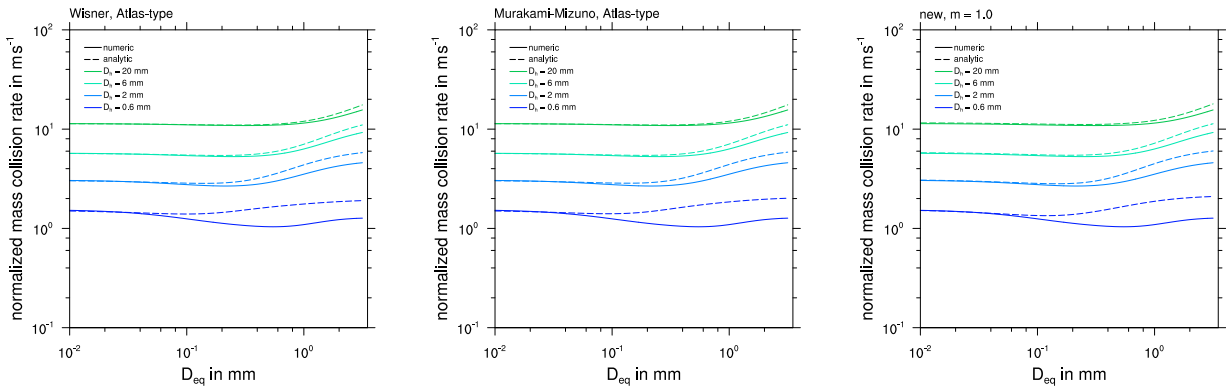
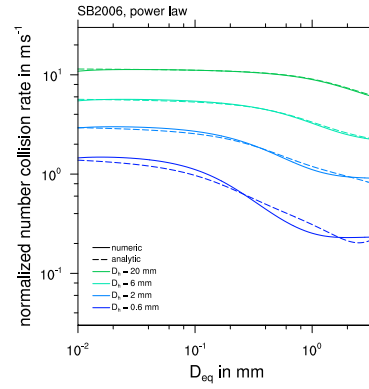
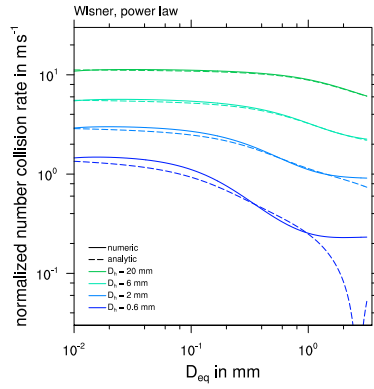


Fig. 12. Normalized mass collision rate for **hail** and **snow** using different approximations (dashed) compared to a numerical solution of the collision integral (solid) as a function of the equivalent mean volume diameter of snowflakes for different mean volume diameters of the hail size distribution.

a) Wisner approx. with power-law

b) SB2006 using power-law



c) Wisner approx. with Atlas-type

d) Murakami-Mizuno with Atlas-type

e) Variance approx. using Atlas-type

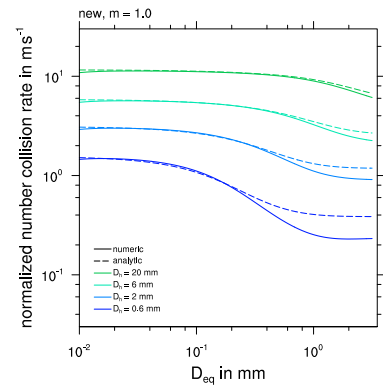
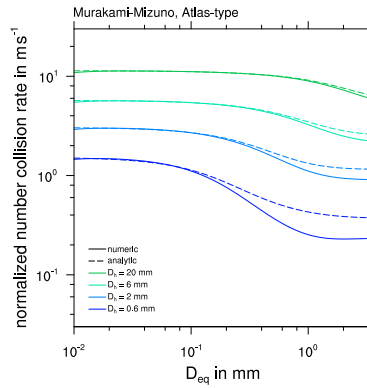
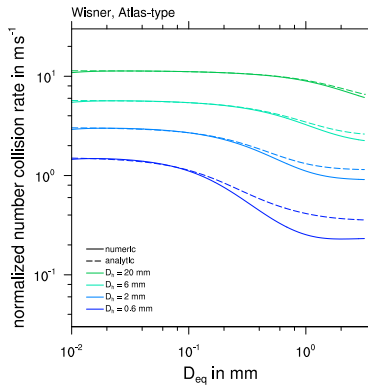
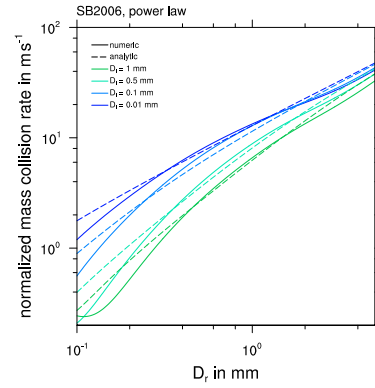
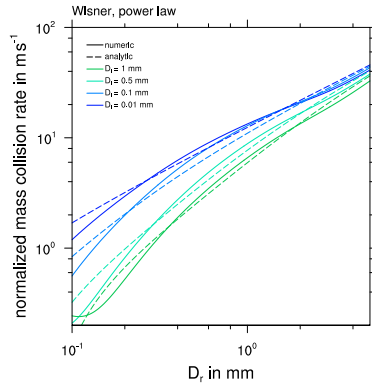


Fig. 13. As previous Figure, but showing the normalized number collision rate for **hail** and **snow**.

a) Wisner approx. using power-law

b) SB2006 using power-law



c) Wisner approx. using Atlas-type

d) Murakami-Mizuno using Atlas-type

e) Variance approx. using Atlas-type

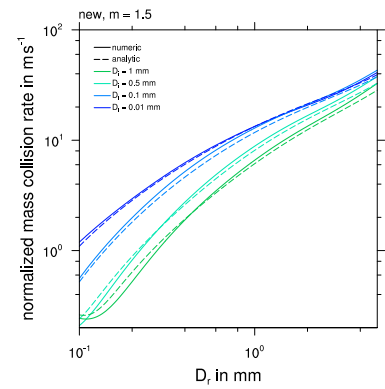
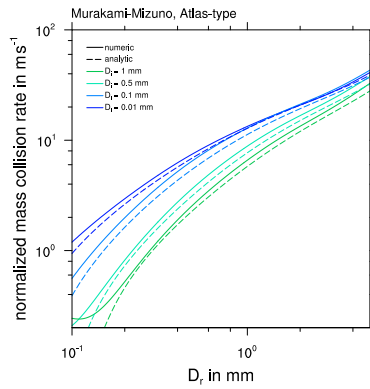
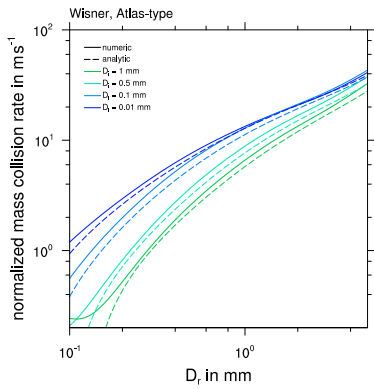
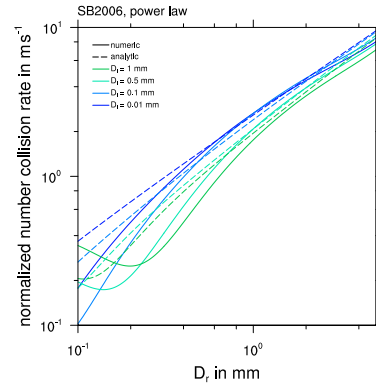
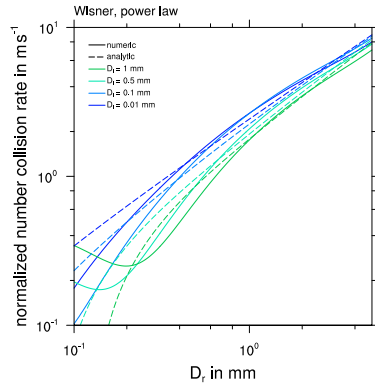


Fig. 14. Normalized mass collision rate for **cloud ice** and **rain** using different approximations (dashed) compared to a numerical solution of the collision integral (solid) as a function of the raindrop mean volume diameter for different mean volume diameters of the cloud ice size distribution.

a) Wisner approx. with power-law

b) SB2006 using power-law



c) Wisner approx. with Atlas-type

d) Murakami-Mizuno with Atlas-type

e) Variance approx. using Atlas-type

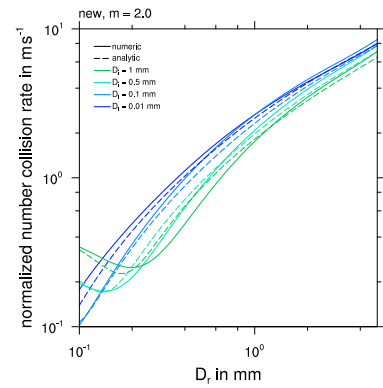
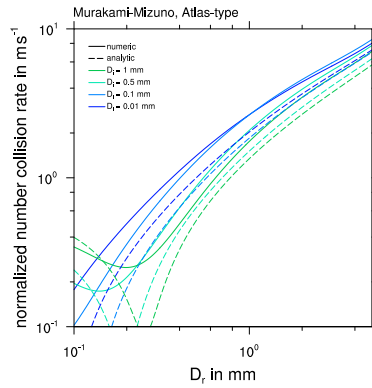
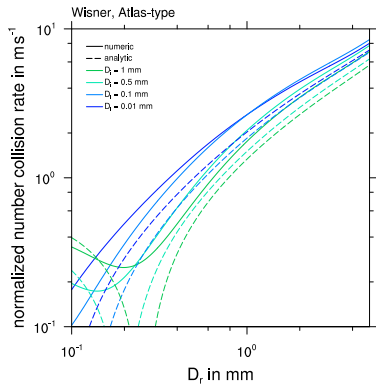
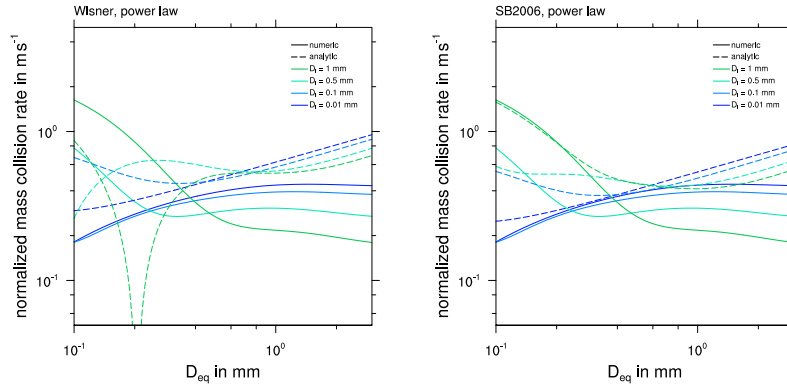


Fig. 15. As previous Figure, but showing the normalized number collision rate for **cloud ice** and **rain**.

a) Wisner approx. using power-law

b) SB2006 using power-law



c) Wisner approx. using Atlas-type

d) Murakami-Mizuno using Atlas-type

e) Variance approx. using Atlas-type

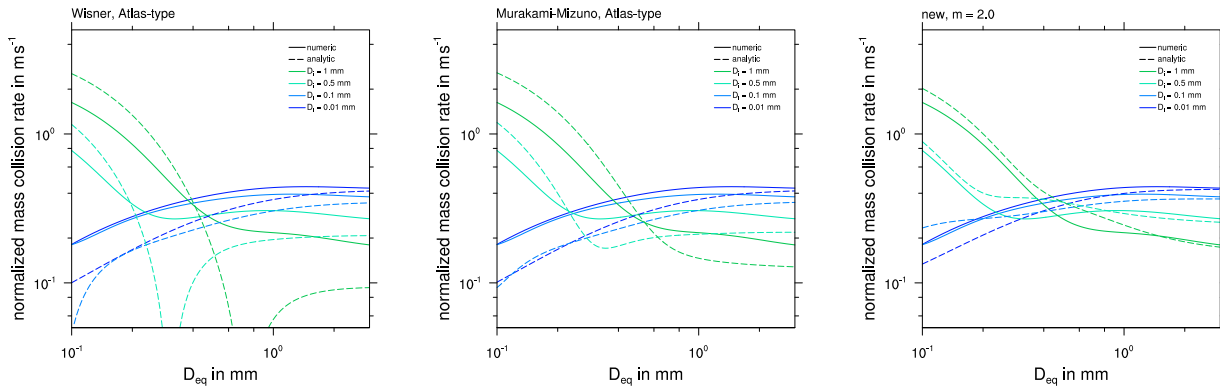
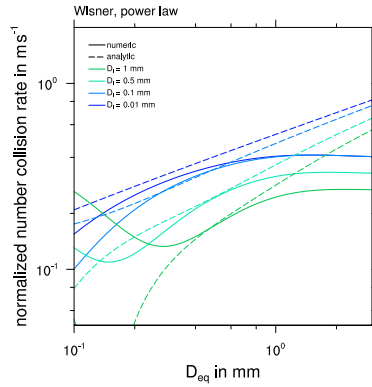
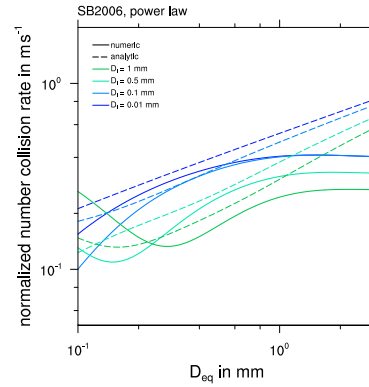


Fig. 16. Normalized mass collision rate for **cloud ice** and **snow** using different approximations (dashed) compared to a numerical solution of the collision integral (solid) as a function of the equivalent mean volume diameter of snowflakes for different mean volume diameters of the cloud ice size distribution.

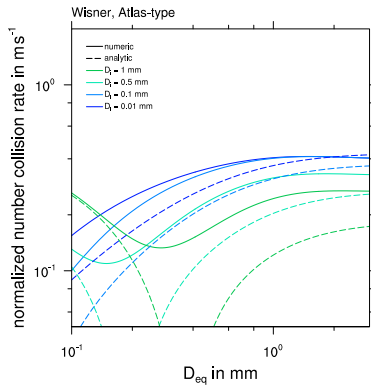
a) Wisner approx. with power-law



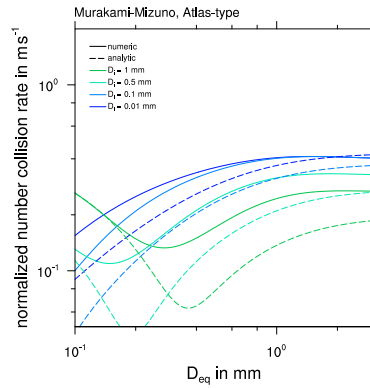
b) SB2006 using power-law



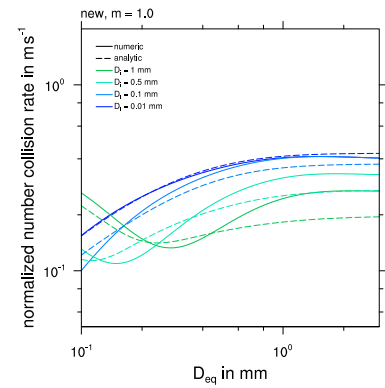
c) Wisner approx. with Atlas-type



d) Murakami-Mizuno with Atlas-type

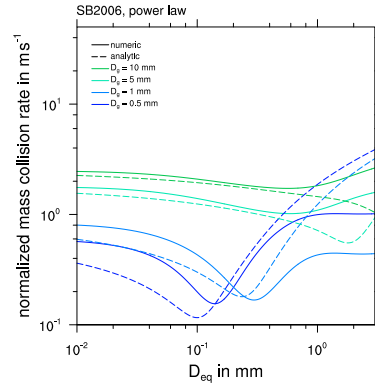
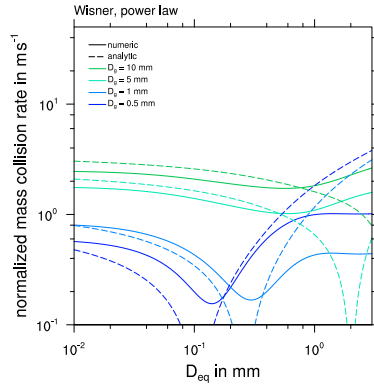


e) Variance approx. using Atlas-type

**Fig. 17.** As previous Figure, but showing the normalized number collision rate for **ice** and **snow**.

a) Wisner approx. using power-law

b) SB2006 using power-law



c) Wisner approx. using Atlas-type

d) Murakami-Mizuno using Atlas-type

e) Variance approx. using Atlas-type

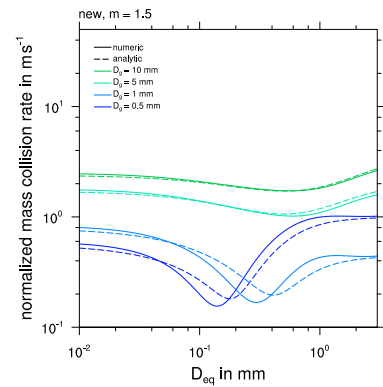
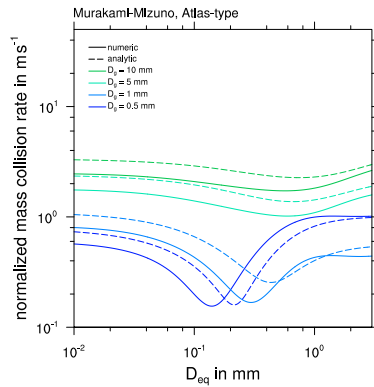
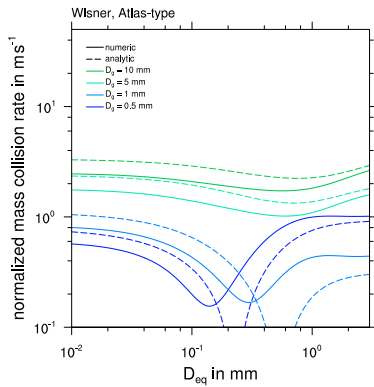
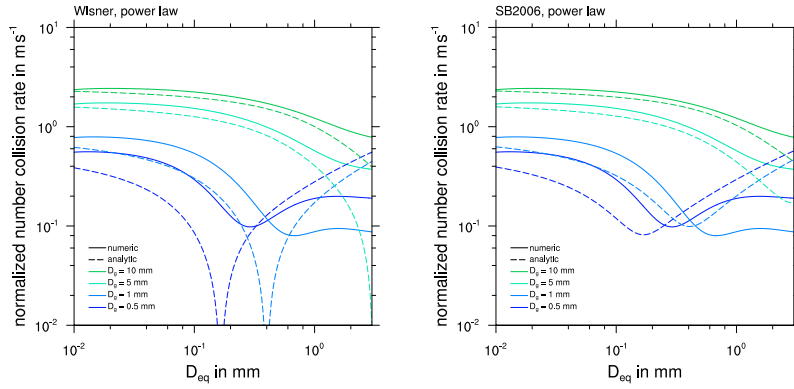


Fig. 18. Normalized mass collision rate for **graupel** and **snow** using different approximations (dashed) compared to a numerical solution of the collision integral (solid) as a function of the equivalent mean volume diameter of snowflakes for different mean volume diameters of the graupel size distribution.

a) Wisner approx. with power-law

b) SB2006 using power-law



c) Wisner approx. with Atlas-type

d) Murakami-Mizuno with Atlas-type

e) Variance approx. using Atlas-type

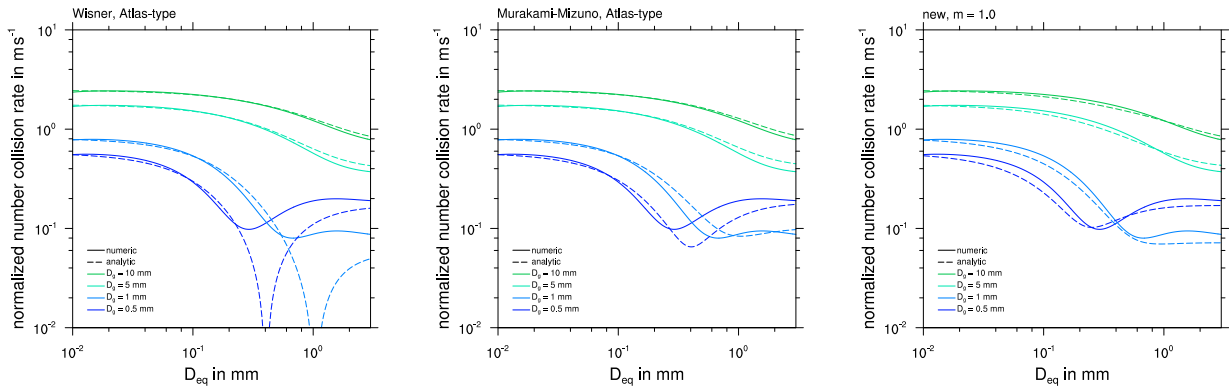


Fig. 19. As previous Figure, but showing the normalized number collision rate for **graupel** and **snow**.

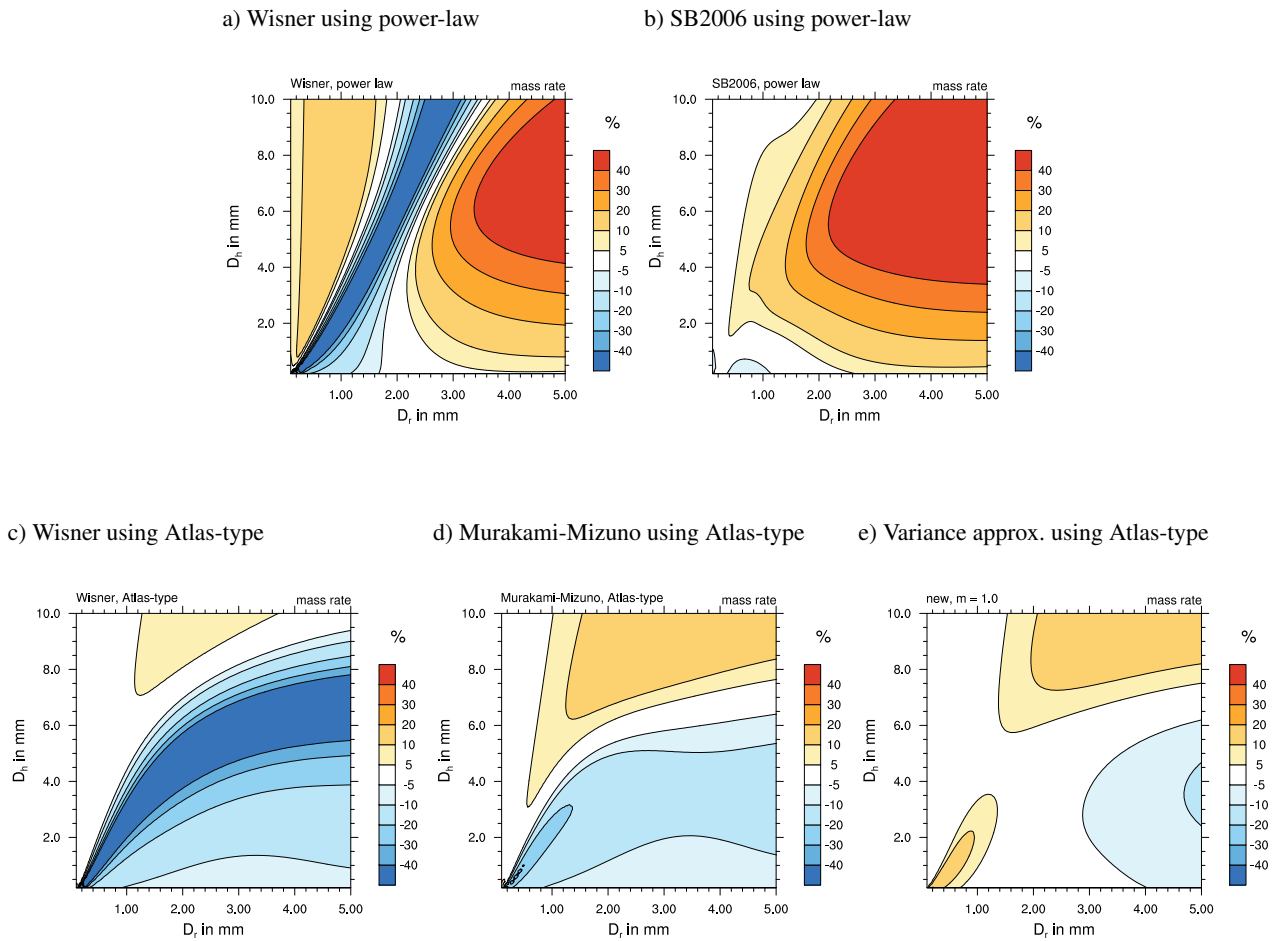


Fig. 20. Symmetric percentage error for the mass collision rate of **hail** and **rain** using different approximations. The numerical solution of the collision integral is used as the reference.

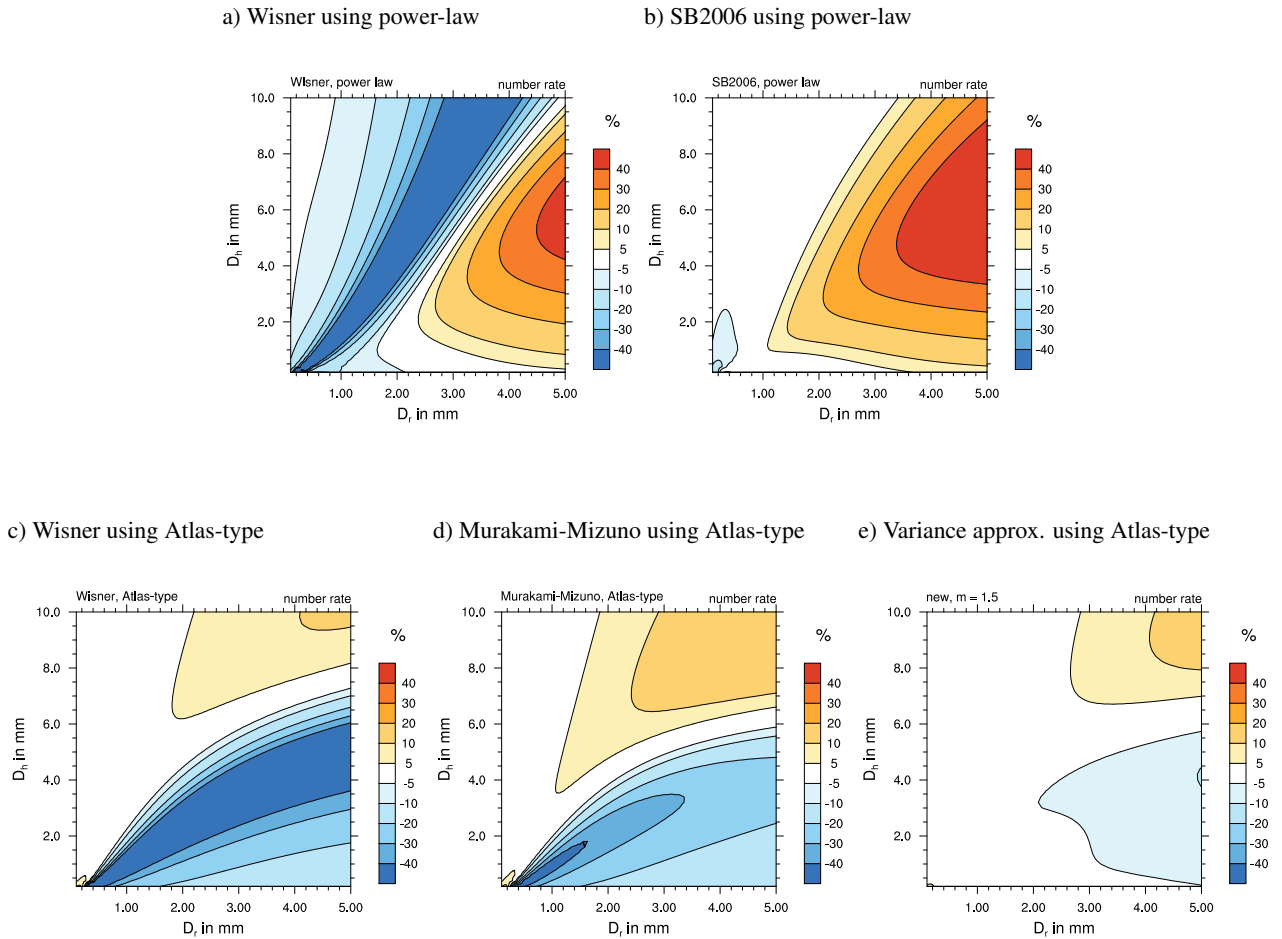
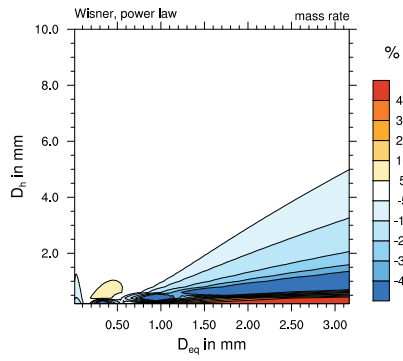
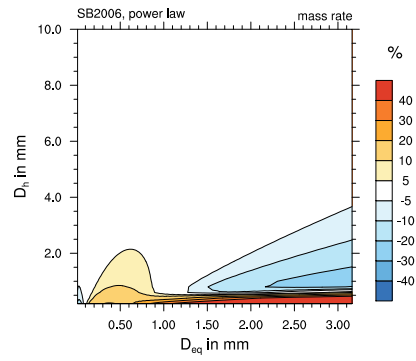


Fig. 21. As previous Figure, but showing the error of the number collision rate for **hail** and **rain**.

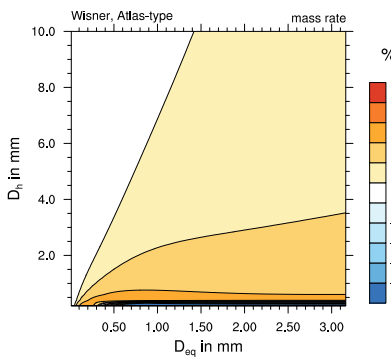
a) Wisner using power-law



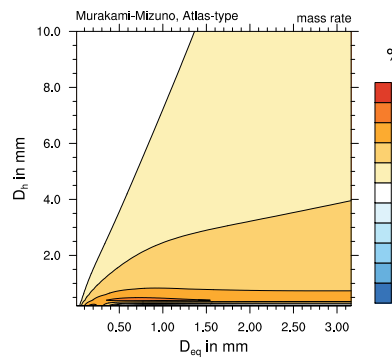
b) SB2006 using power-law



c) Wisner using Atlas-type



d) Murakami-Mizuno using Atlas-type



e) Variance approx. using Atlas-type

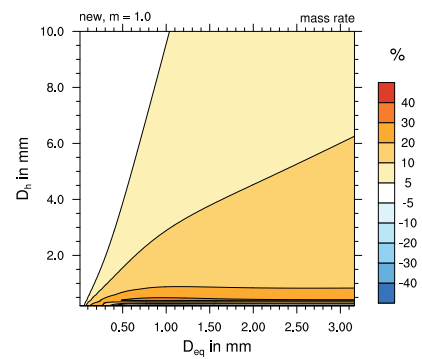


Fig. 22. Symmetric percentage error for the mass collision rate of hail and snow using different approximations. The numerical solution of the collision integral is used as the reference.

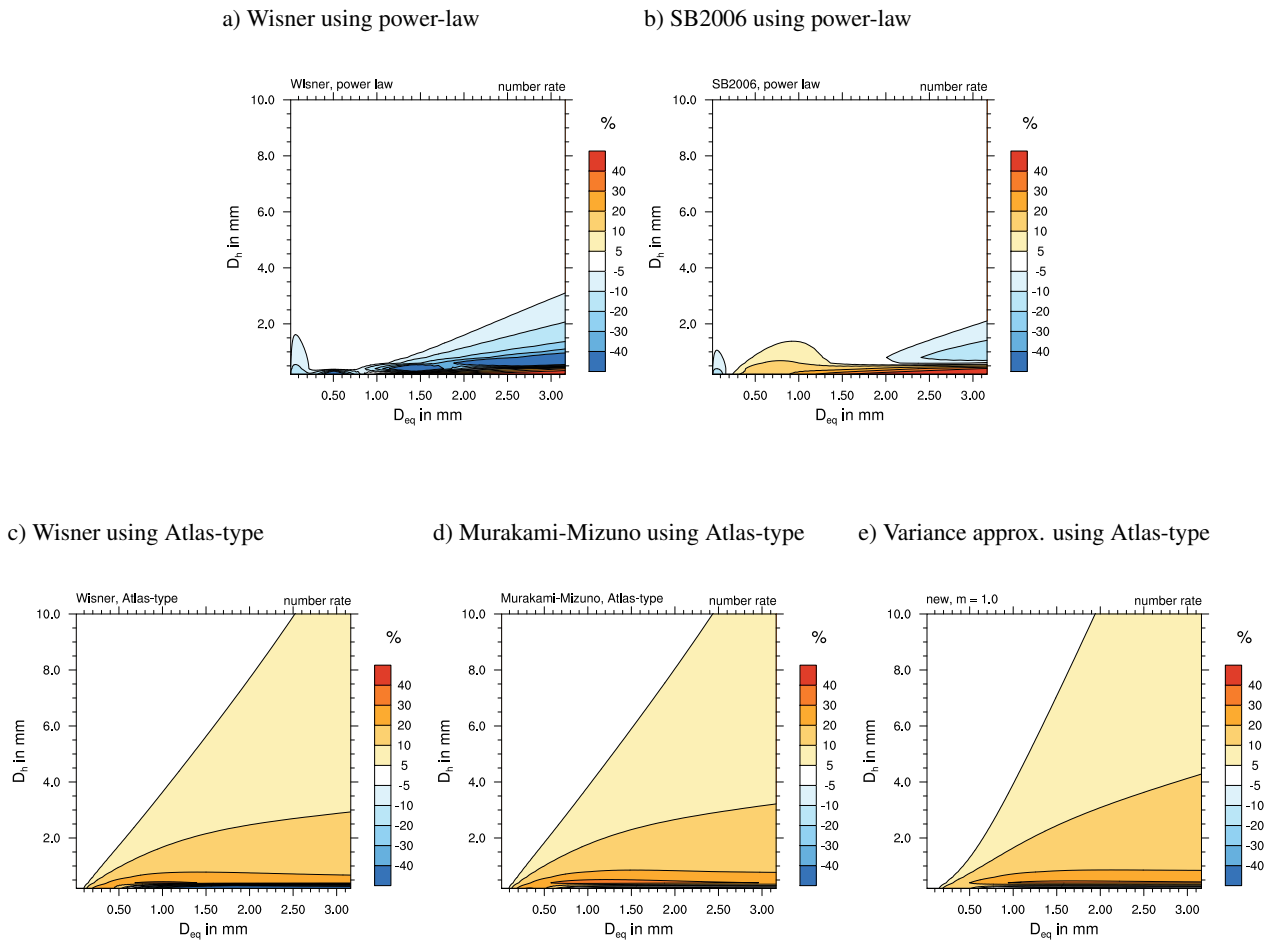


Fig. 23. As previous Figure, but showing the error of the number collision rate for **hail** and **snow**.

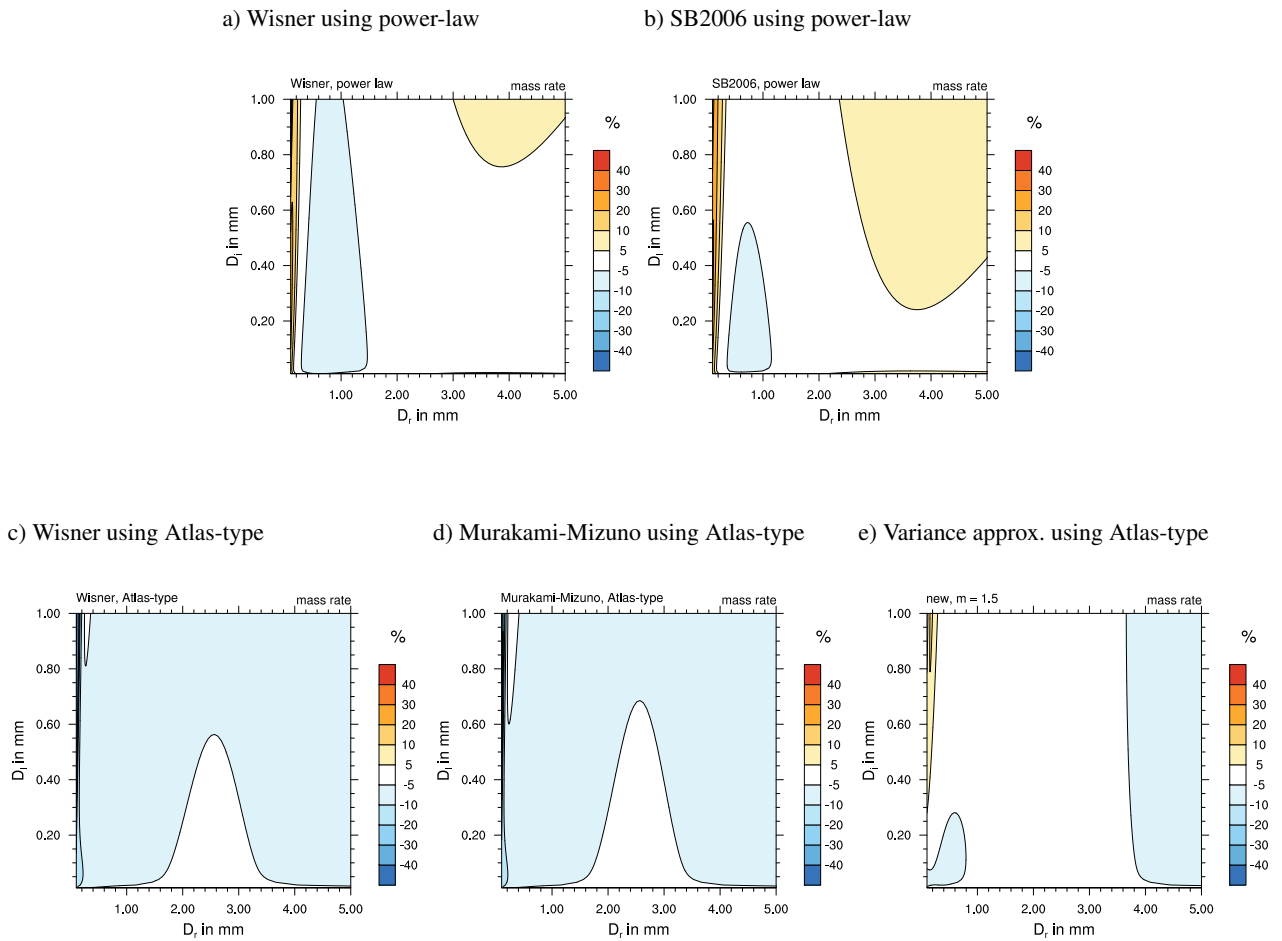


Fig. 24. Symmetric percentage error for the mass collision rate of **cloud ice** and **rain** using different approximations. The numerical solution of the collision integral is used as the reference.

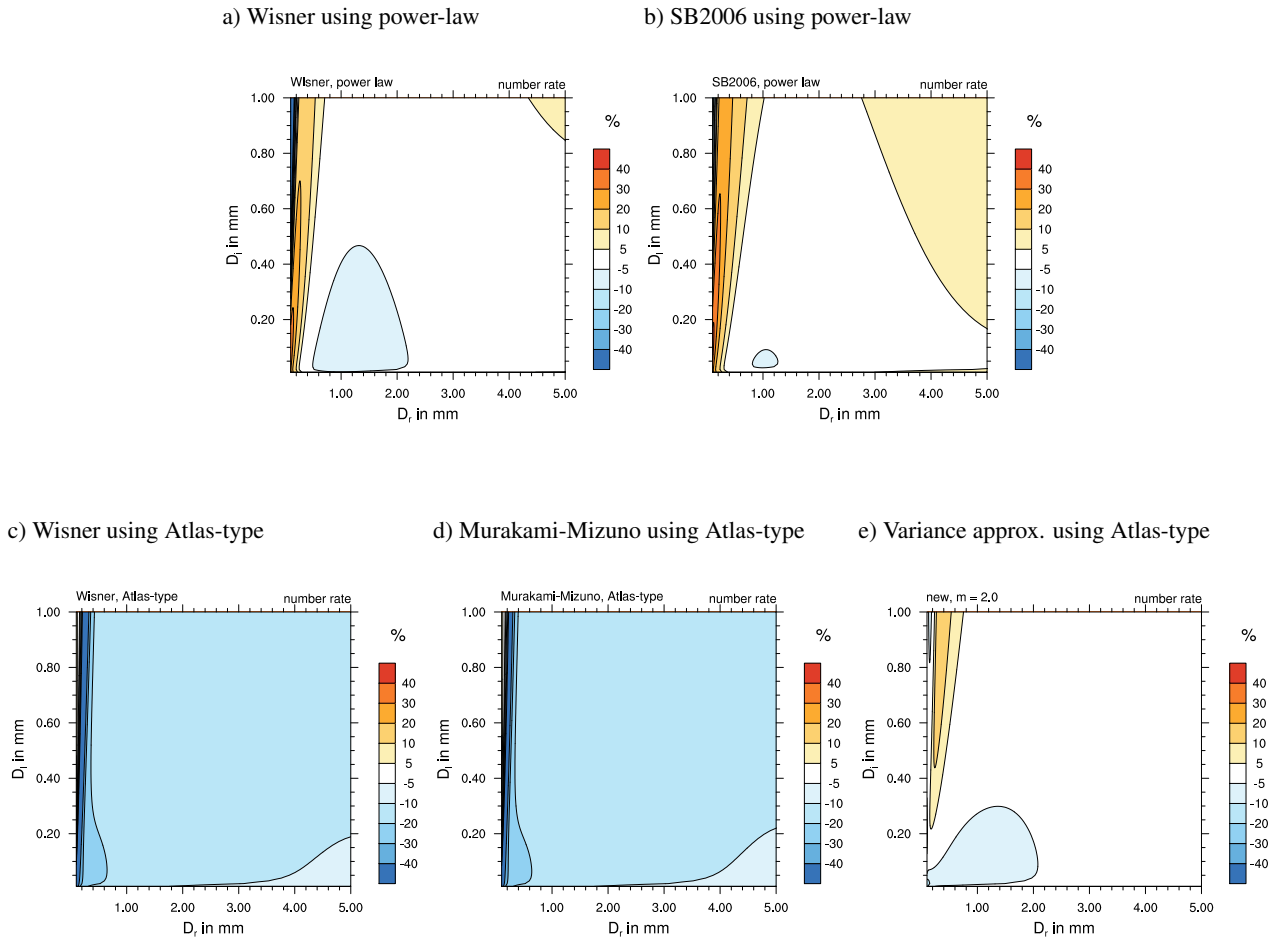


Fig. 25. As previous Figure, but showing the error of the number collision rate for **cloud ice** and **rain**.

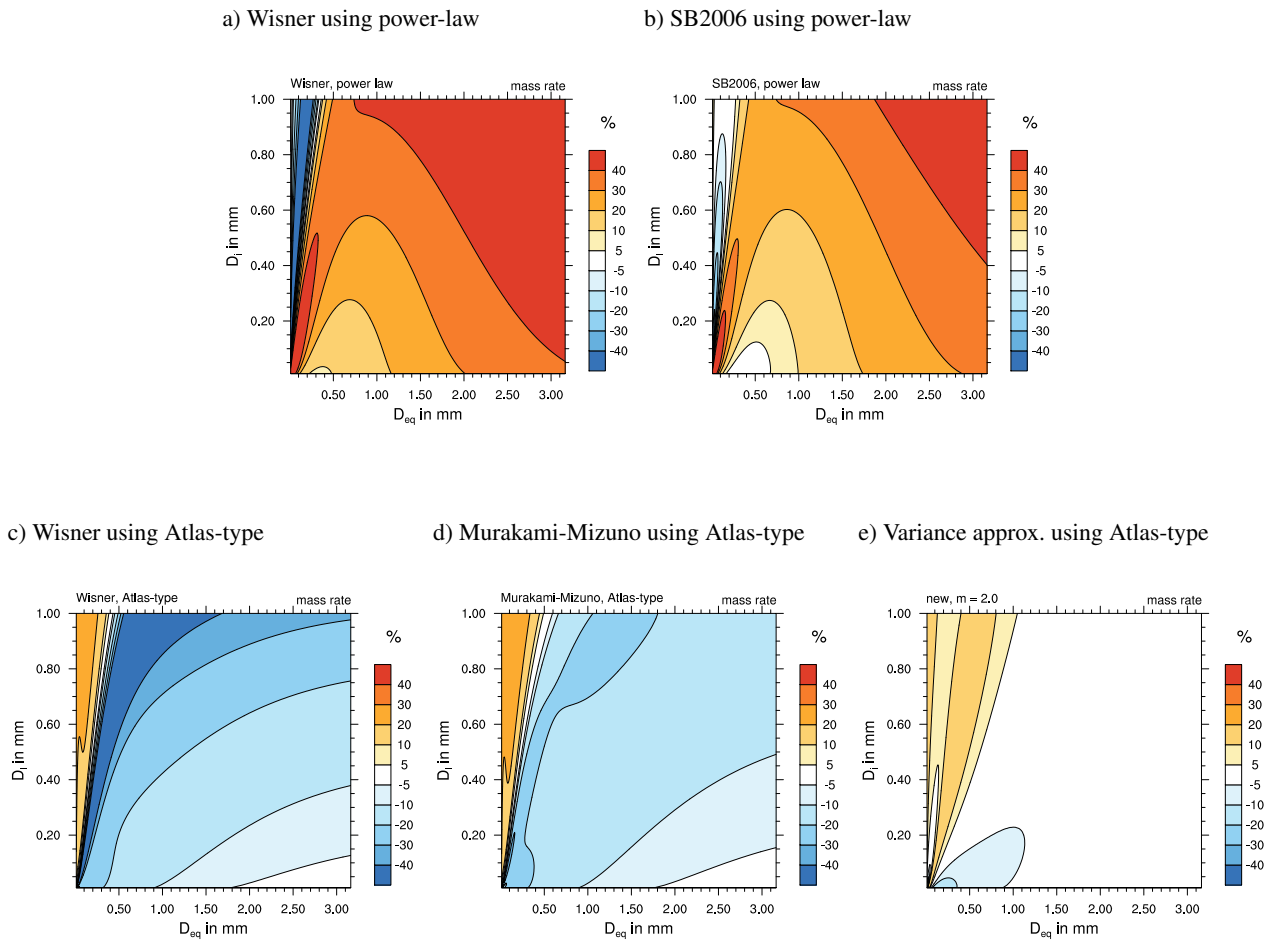


Fig. 26. Symmetric percentage error for the mass collision rate of **cloud ice** and **snow** using different approximations. The numerical solution of the collision integral is used as the reference.

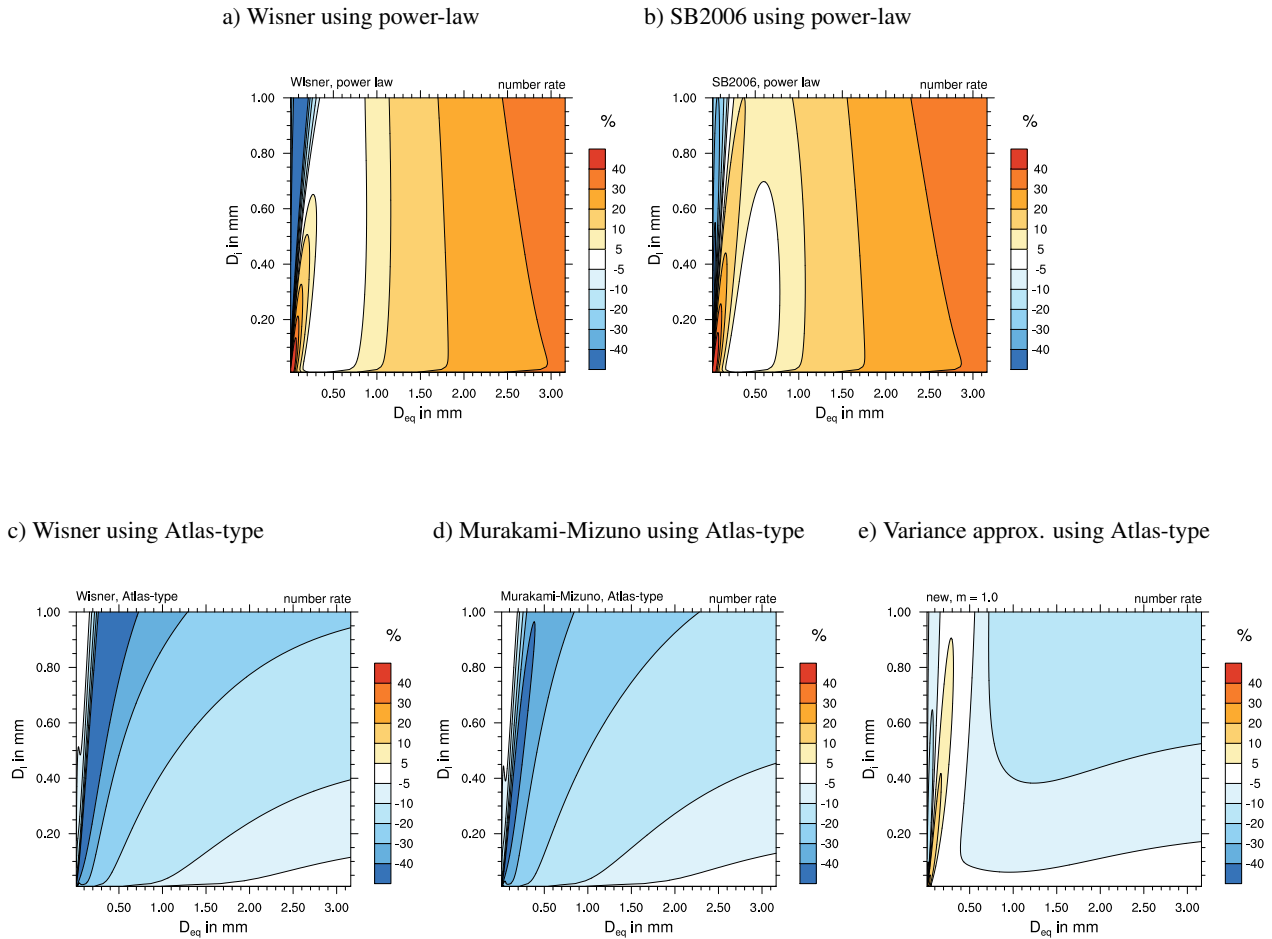


Fig. 27. As previous Figure, but showing the error of the number collision rate for **cloud ice and snow**.

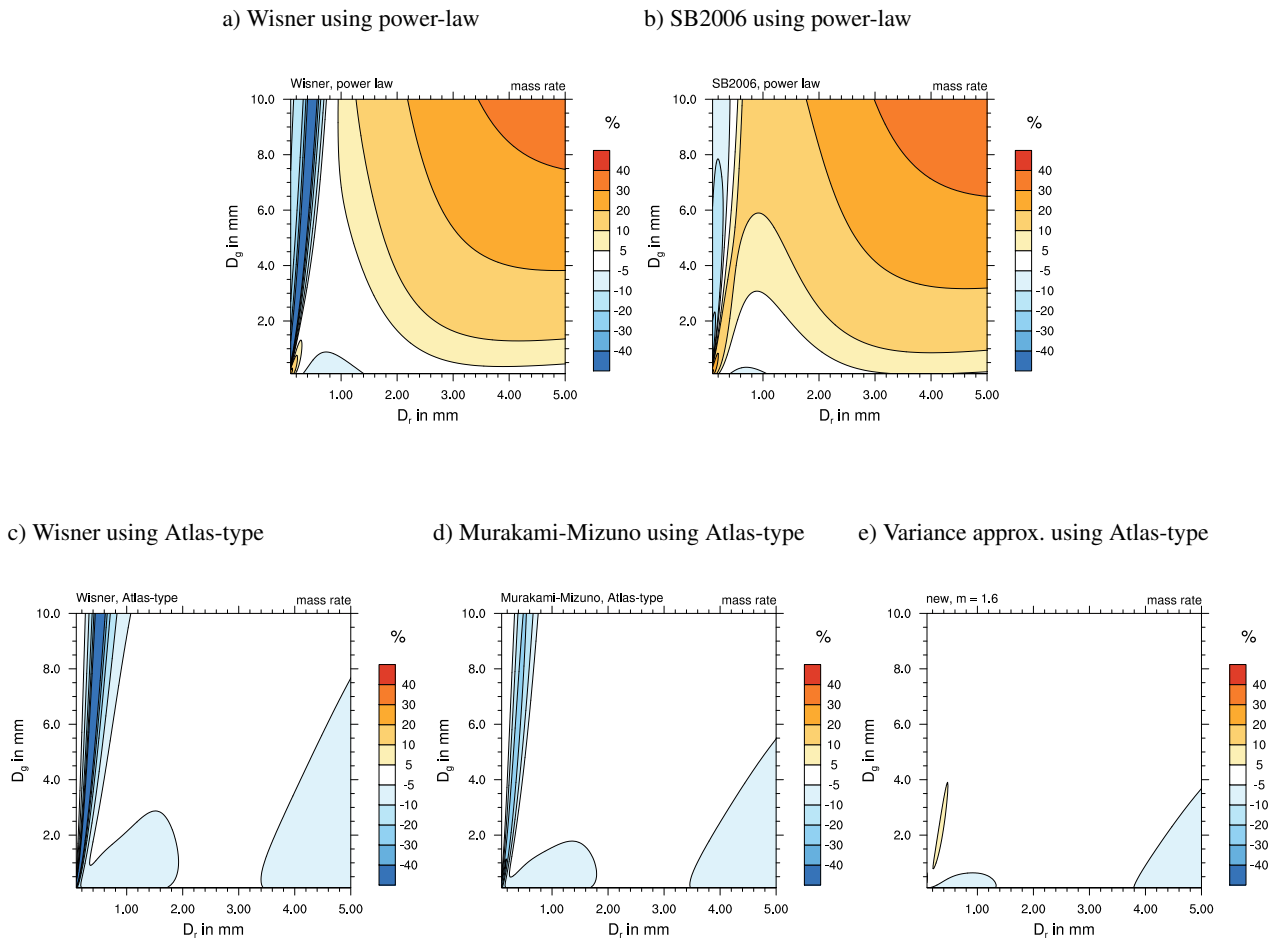


Fig. 28. Symmetric percentage error for the mass collision rate of **graupel** and **rain** using different approximations. The numerical solution of the collision integral is used as the reference.

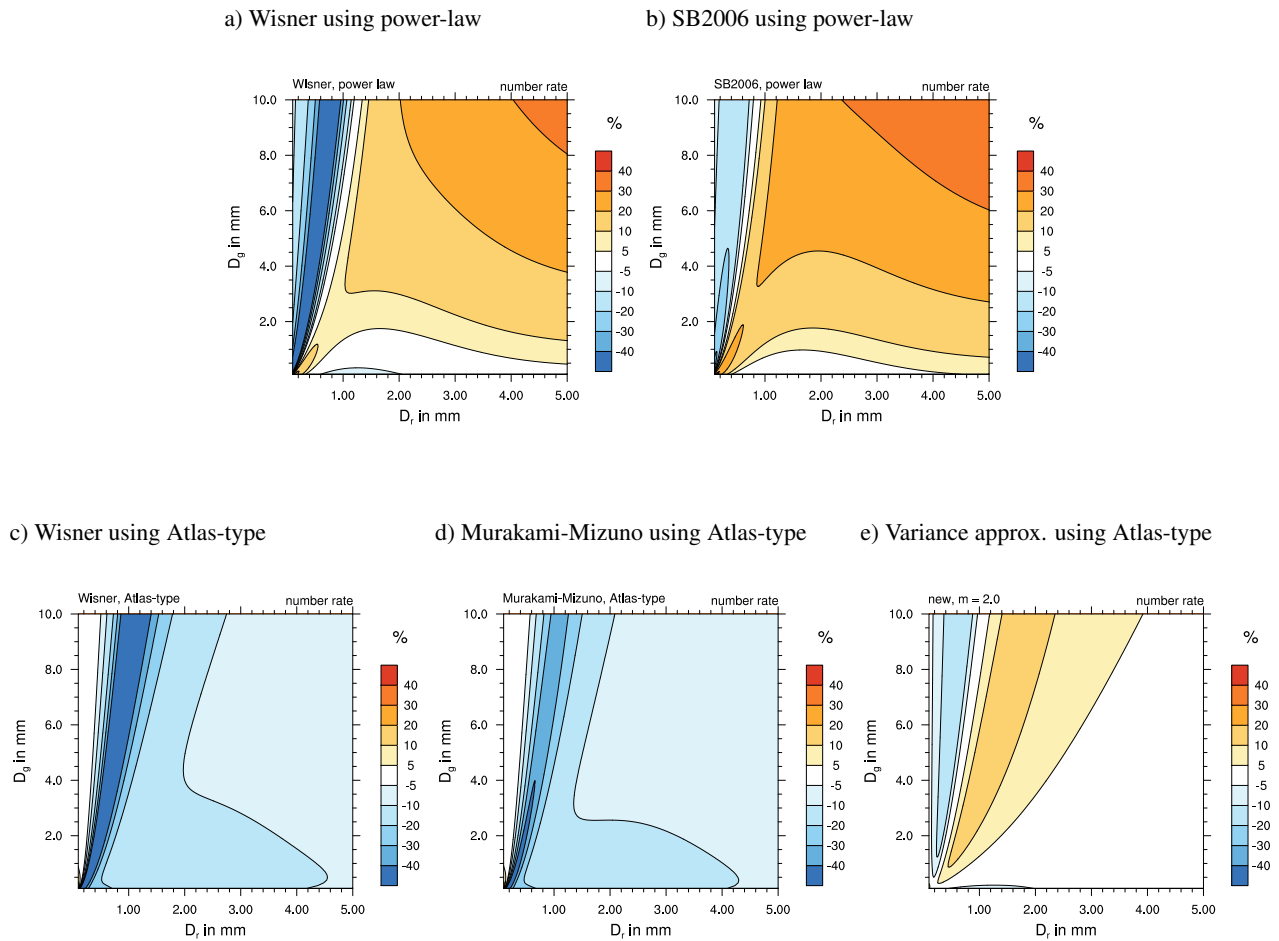


Fig. 29. As previous Figure, but showing the error of the number collision rate for **graupel** and **rain**.

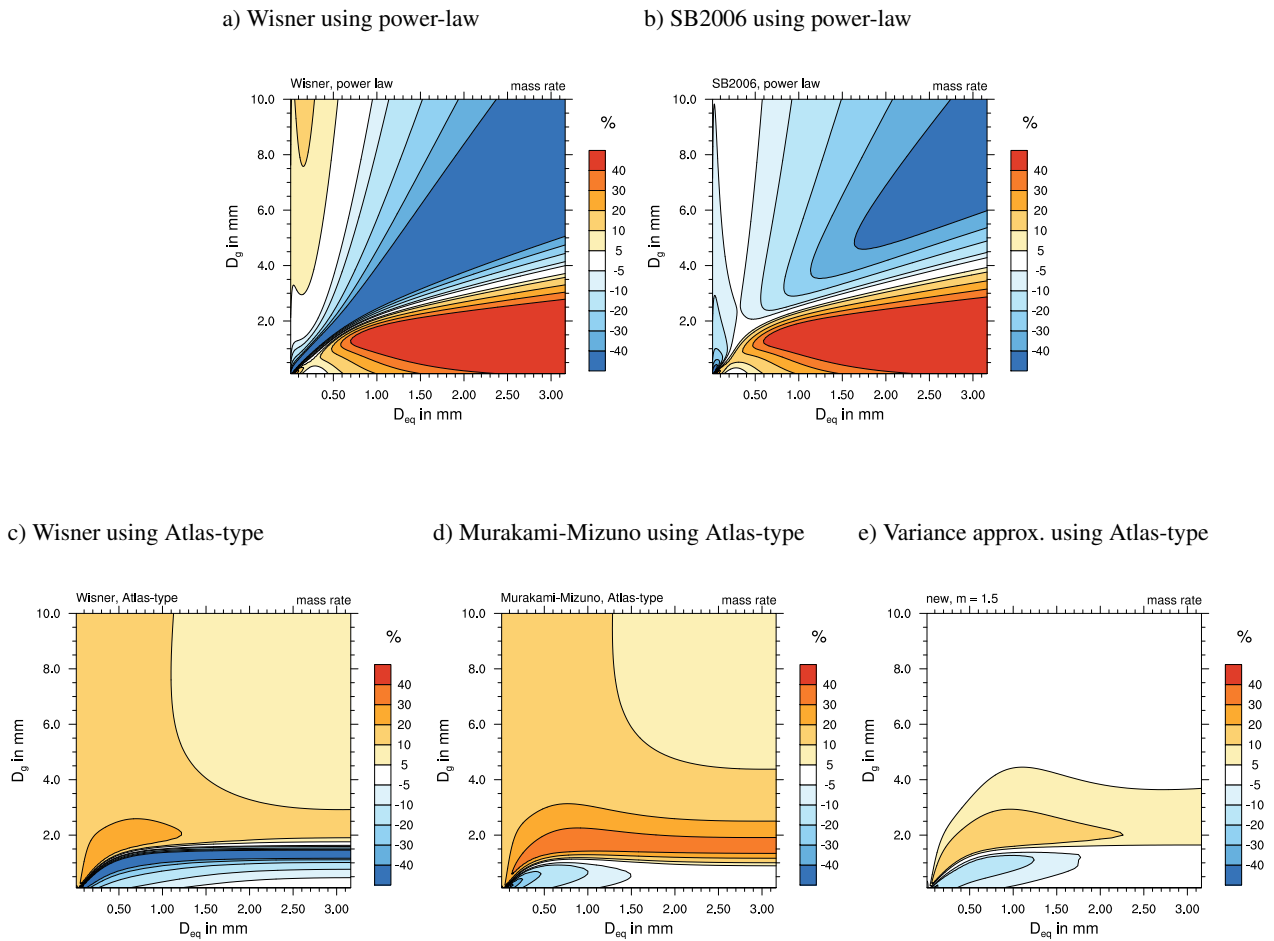


Fig. 30. Symmetric percentage error for the mass collision rate of **graupel** and **snow** using different approximations. The numerical solution of the collision integral is used as the reference.

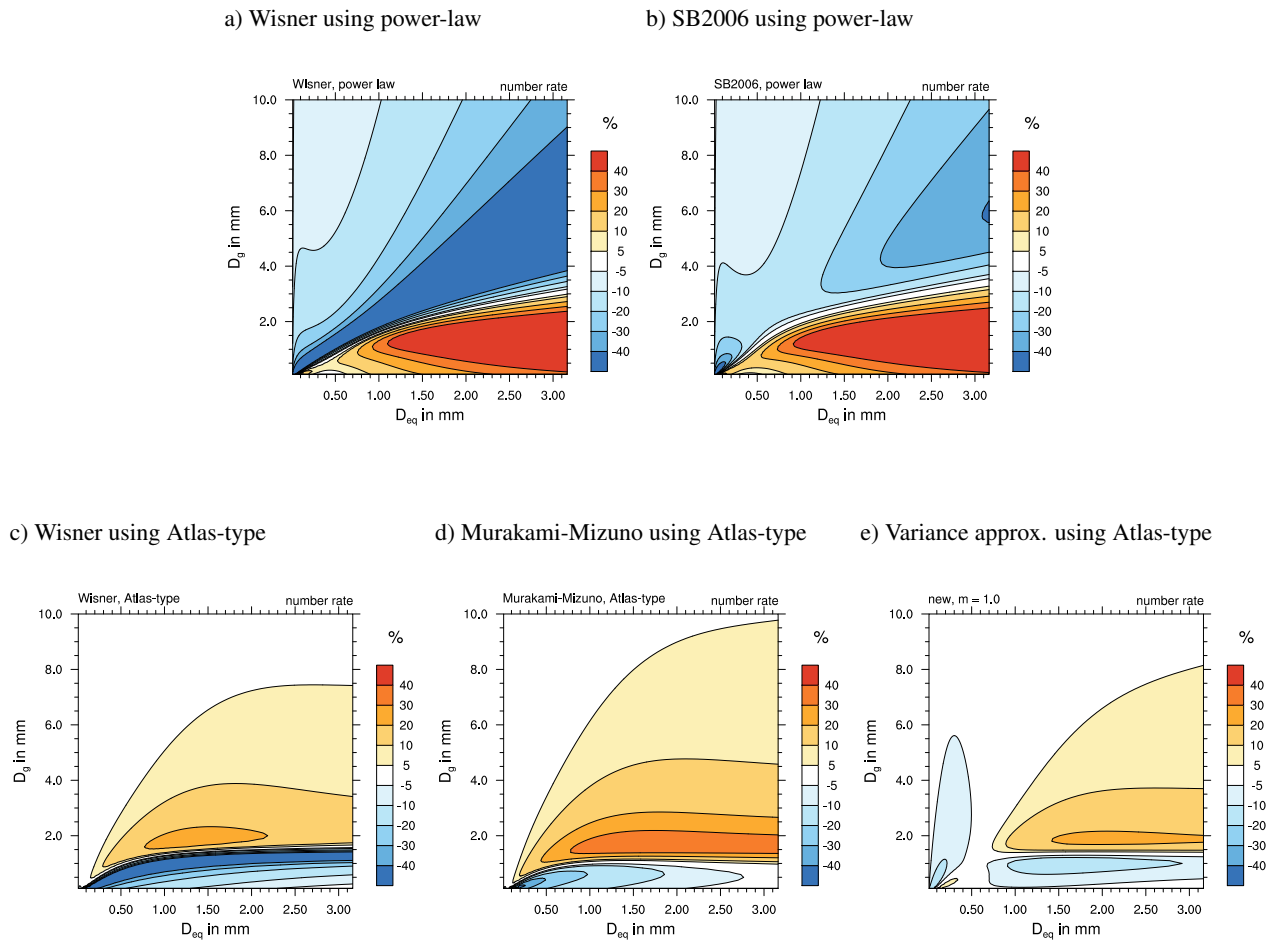
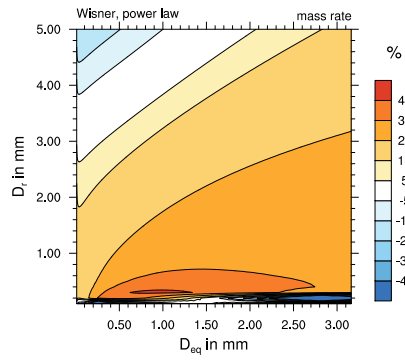
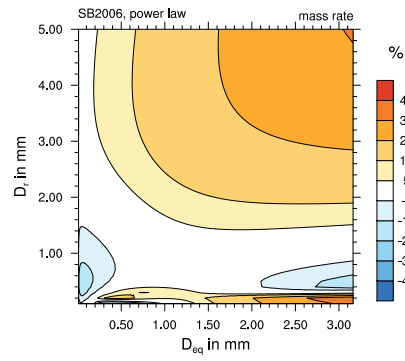


Fig. 31. As previous Figure, but showing the error of the number collision rate for **graupel** and **snow**.

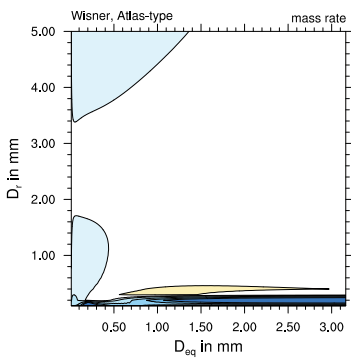
a) Wisner using power-law



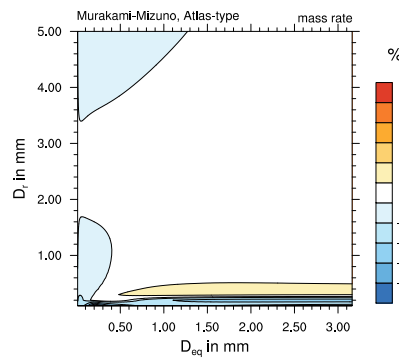
b) SB2006 using power-law



c) Wisner using Atlas-type



d) Murakami-Mizuno using Atlas-type



e) Variance approx. using Atlas-type

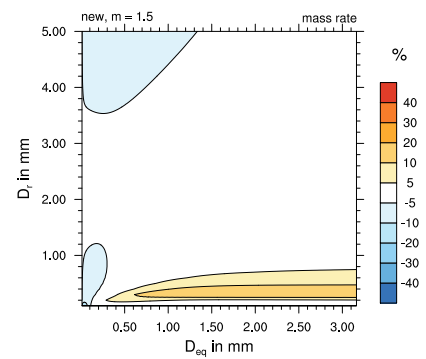


Fig. 32. Symmetric percentage error for the mass collision rate of rain and snow using different approximations. The numerical solution of the collision integral is used as the reference.

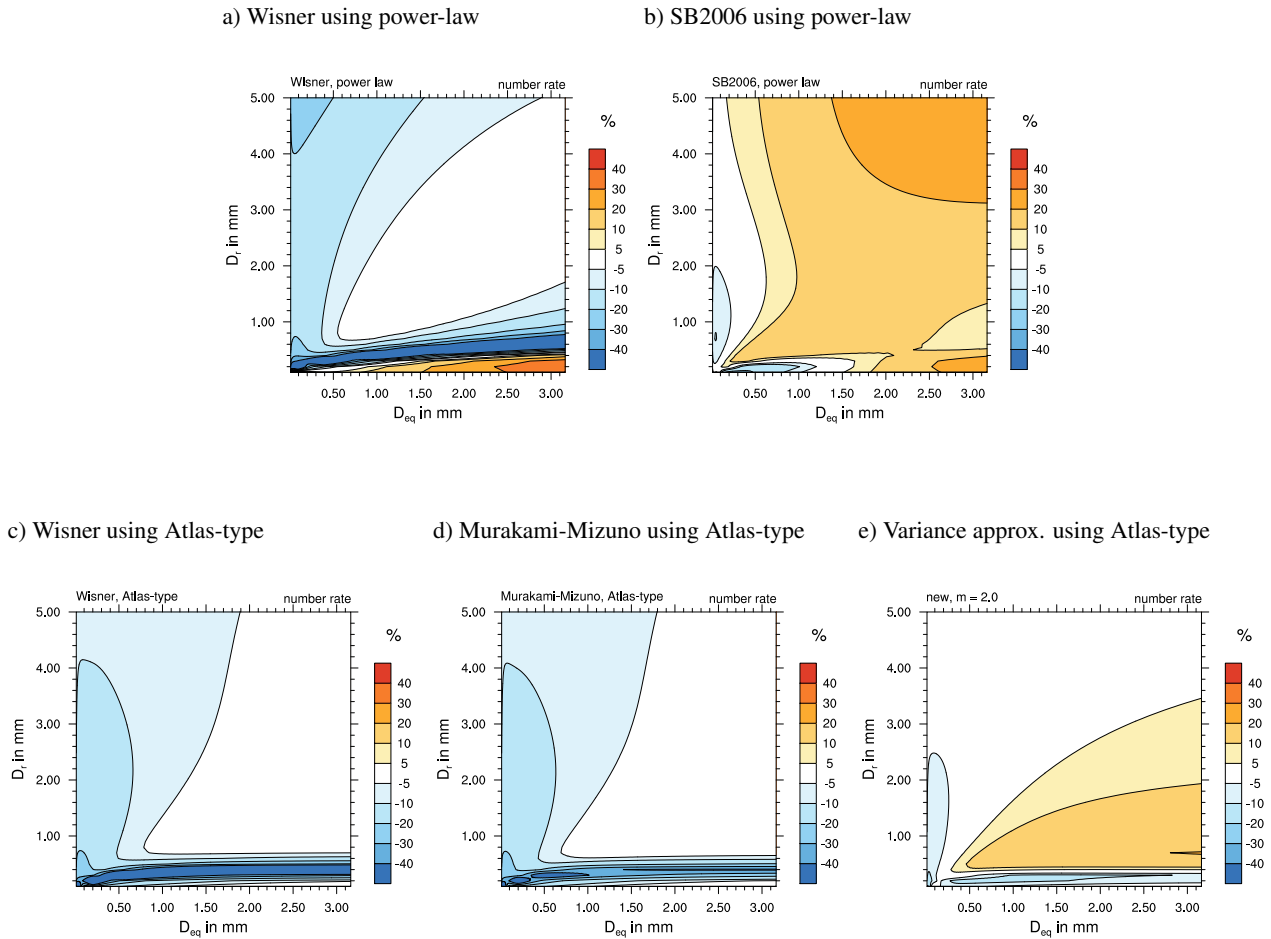
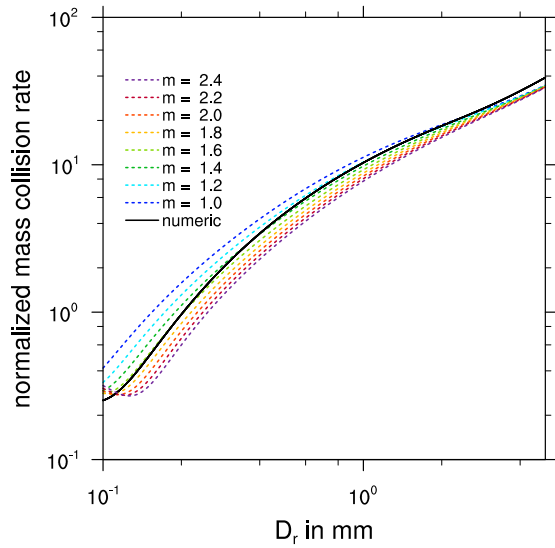
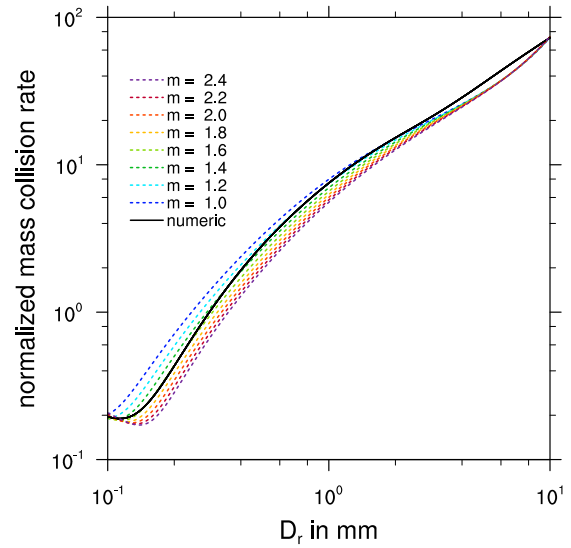


Fig. 33. As previous Figure, but showing the error of the number collision rate for **rain** and **snow**.

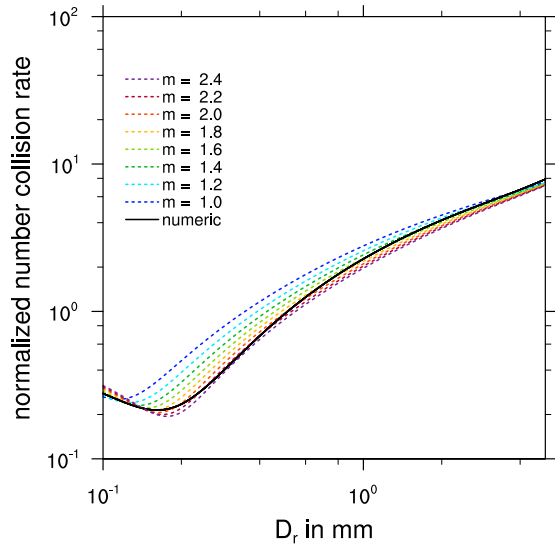
a) graupel-rain mass collection rate



b) snow-rain mass collection rate



a) graupel-rain number collection rate



b) snow-rain number collection rate

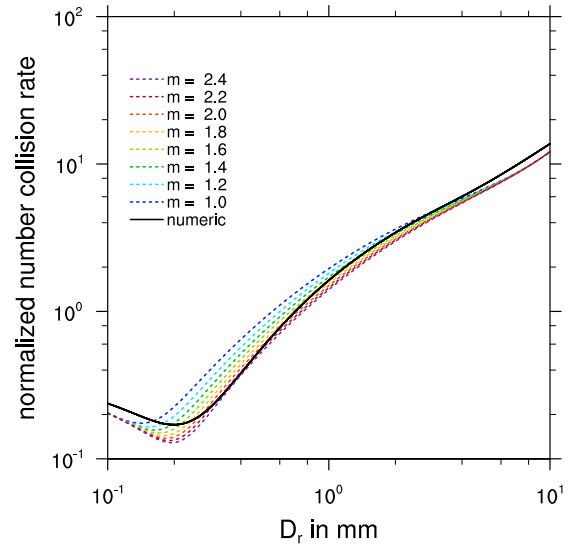
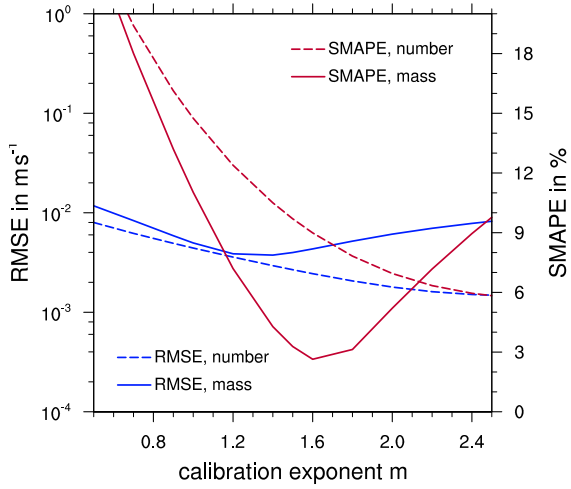
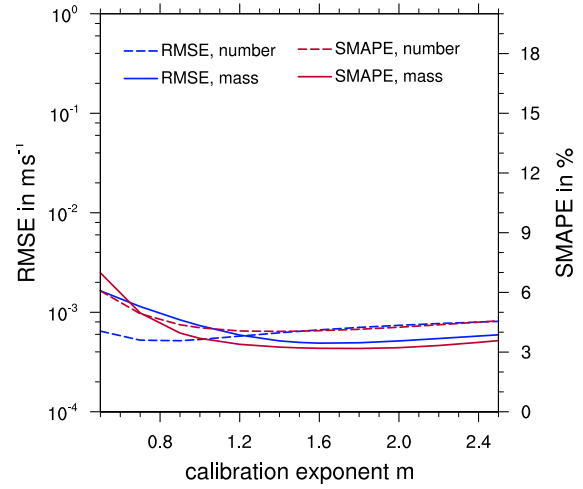


Fig. 34. Normalized bulk collision rates of mass and number for the graupel-rain as well as snow-rain collection. Shown is the dependency on the calibration exponent m (colors) in comparison with the reference solution using numerical integration (black solid line).

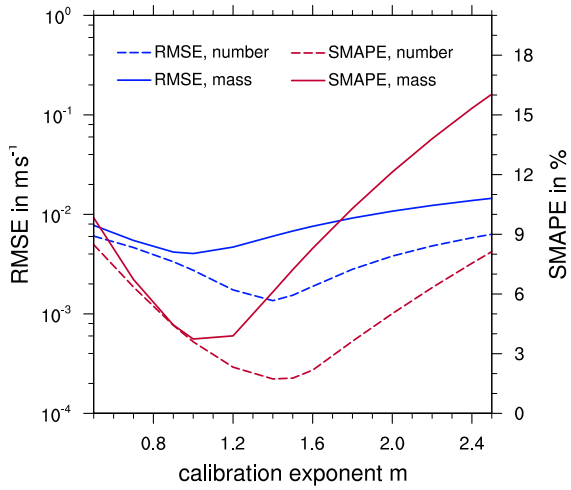
a) graupel-rain collection



b) graupel-snow collection



c) hail-rain collection



d) hail-snow collection

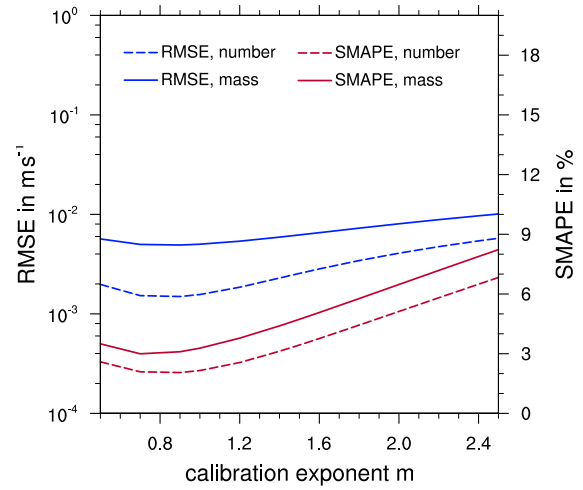
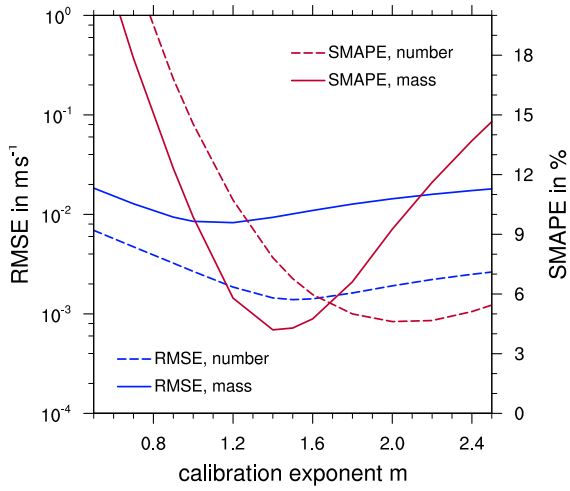
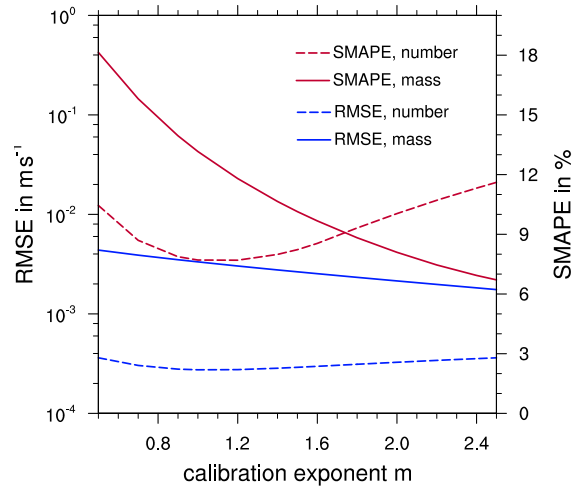


Fig. 35. Error measures (RMSE and SMAPE) of the revised variance approximation as a function of the calibration exponents m for various collection rates. Shown is the root mean squared error (RMSE) and the symmetric mean absolute percentage error (SMAPE).

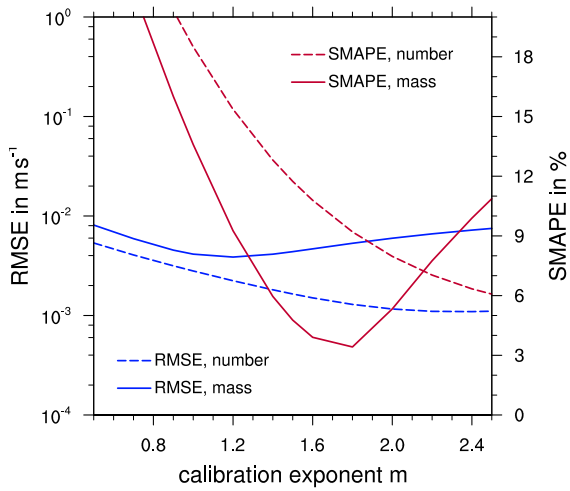
a) ice-rain collection



b) ice-snow collection



c) snow-rain collection



b) snow self-collection

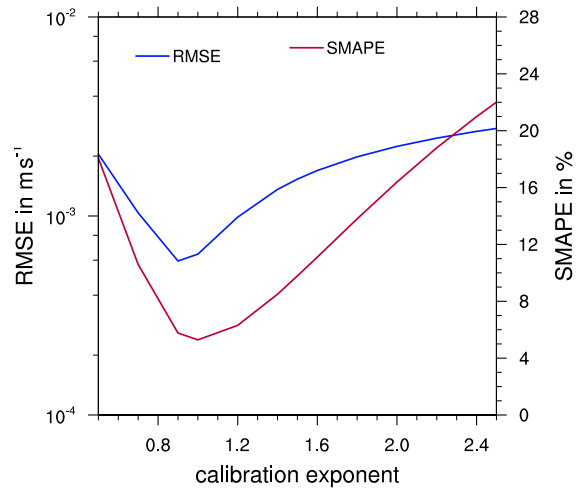
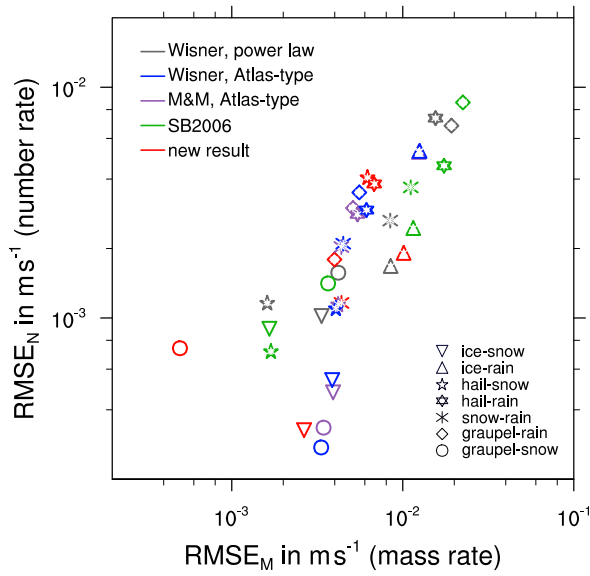


Fig. 36. As Fig. 35, but showing the results for other collection rates including the selfcollection of snow.

a) RMSE



b) SMAPE

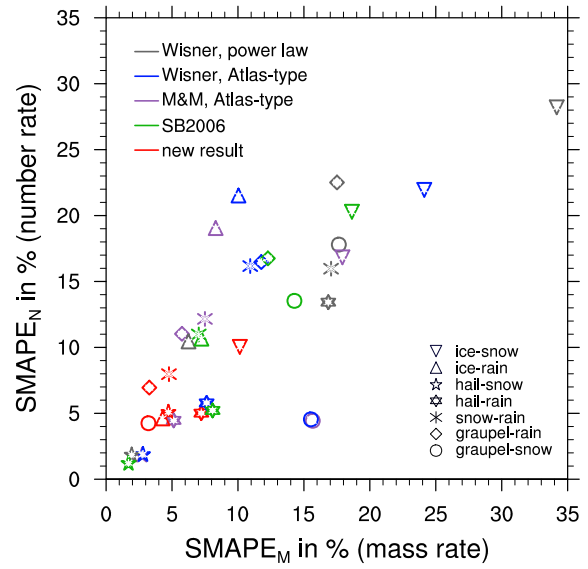


Fig. 37. Root mean square error (RMSE, left) and symmetric mean absolute percentage error (SMAPE, right) of the normalized bulk number and mass collection rates for seven different binary collision interactions using $m = 1.5$ for mass and $m = 2$ for number for all collision rates (instead of applying the 'optimal' values).